



# 1 Have you ever seen the rain? Observing a record 2 convective rainfall with national and local monitoring 3 networks and opportunistic sensors

4 Louise Petersson Wårdh<sup>1,2\*</sup>, Hasan Hosseini<sup>1,2</sup>, Remco van de Beek<sup>2</sup>, Jafet C.M. Andersson<sup>2</sup>,  
5 Hossein Hashemi<sup>1</sup>, Jonas Olsson<sup>1,2</sup>

6 <sup>1</sup> Division of Water Resources Engineering, Faculty of Engineering, Lund University, P.O. Box  
7 118, 22100 Lund, Sweden

8 <sup>2</sup> Swedish Meteorological and Hydrological Institute (SMHI), Folkborgsvägen 17, Norrköping  
9 SE-601 76, Sweden

10 \*Corresponding author. E-mail: louise.petersson\_wardh@tvrl.lth.se.

## 11 Abstract

12 Short-duration extreme rainfall can cause severe impacts in built environments and flood  
13 mitigation measures require high-resolution rainfall data to be effective. It is a particular  
14 challenge to observe convective storms which are expected to intensify with climate change.  
15 However, rainfall monitoring networks operated by national meteorological and hydrological  
16 services generally have limited ability to observe rainfall at sub-hourly and sub-kilometre scale.  
17 This paper investigates the capability of second- and third-party rainfall sensors to observe a  
18 highly localized convective storm that hit southwestern Sweden in August 2022. Specifically,  
19 we compared the observations from professional weather stations, C-band radar, X-band  
20 radar, Commercial Microwave Links and Personal Weather Stations to get a full impression of  
21 the sensors' strengths and weaknesses in the context of convective storms. The results  
22 suggest that second- and third-party networks can contribute with important information on  
23 short-duration extreme rainfall to national weather services. The second-party network  
24 assisted in quantifying the magnitude and spatial variability of the event with high precision.  
25 The third-party network could contribute to the understanding of the duration and spatial  
26 distribution of the storm, but underestimated the magnitude compared with the reference  
27 sensors.

## 28 1. Introduction

29 The global trend of urbanization is increasingly exposing people and assets to flood risks,  
30 which particularly affects the urban poor (Winsemius et al., 2018; Petersson et al., 2020; UN-  
31 Habitat, 2024). Flood mitigation and disaster preparedness measures require rainfall  
32 measurements on sub-hourly and sub-kilometre scale to be effective from the planning phase  
33 to post-event analysis (Guo, 2006; Marchi et al., 2009; Mailhot & Duchesne, 2010; Fuentes-



34 Andino et al., 2017; Pulkkinen et al., 2019; Imhoff et al., 2020). However, traditional monitoring  
35 techniques generally have limited ability to accurately observe rainfall at this spatiotemporal  
36 resolution. The most impactful rainfall events in urban areas are typically convective storms,  
37 which can cause heavy rainfall over small areas and short durations with severe damage as  
38 consequence (Kaiser et al., 2021; Mobini et al., 2021).

39 In Sweden, the Swedish Meteorological and Hydrological Institute (SMHI) operates around  
40 600 rain gauges distributed over a land mass of 410,000 km<sup>2</sup>. Of these, around 130 are  
41 automatic stations recording accumulated rainfall depth every 15 minutes and the remaining  
42 are manual stations reporting daily amounts. The station network is complemented with 12 C-  
43 band Weather Radars (CWR) across the country with outputs every 5 minutes at 2 km spatial  
44 resolution. While CWR generally is capable of producing good spatial representation of  
45 precipitation, it has limitations caused by overshooting, beam blockage and clutter (Einfalt et  
46 al., 2004; van de Beek et al., 2016). For highly localized convective events, the spatiotemporal  
47 resolution of Sweden's official gauge network and radar composite is too low to capture  
48 essential rainfall dynamics, such as spatial variability and peak intensity.

49 One option for national weather services to access high-resolution rainfall measurements is to  
50 reach agreements with other professional entities like municipal water utilities and universities  
51 who maintain their own monitoring networks, so-called "second-party data" (Garcia-Marti et al.,  
52 2023). While these data might be trustworthy for operational use, their sampling resolution  
53 may, just like official data, be insufficient on the "unresolved spatial scale" in which convective  
54 storms occur (Lussana et al., 2023). In light of this, SMHI has recently gained interest in  
55 additional external observations not operated by any official agency, sometimes referred to as  
56 "third-party data". The new technologies are often enabled by digitalization and user-generated  
57 content on the Internet, which lowers the barriers and costs associated with data acquisition.  
58 While these data can provide higher resolution observations in space and time, they are often  
59 subject to uncertainties and bias due to the lack of installation guidelines, maintenance  
60 protocols and mechanisms to reinforce such standards. These promises and concerns have  
61 sparked research efforts on applications and quality control of third-party data at SMHI and  
62 many other European meteorological services (Hahn et al., 2022; Garcia-Marti et al., 2023).

63 This paper investigates the capability of second- and third-party rainfall sensors to observe a  
64 highly localized convective storm that occurred on 18 August 2022 in Båstad, Sweden. The  
65 second-party data come from sensors managed by local authorities in southwestern Sweden  
66 and consists of a traditional rain gauge and an X-band Weather Radar (XWR). As for third-  
67 party data, we study rainfall observations from a Commercial Microwave Link (CML) and a set  
68 of Personal Weather Stations (PWS). CML and PWS are sometimes referred to as  
69 "opportunistic sensors" (Fencl et al., 2024). Here, we will use the term "third-party data" for



70 consistency. First, the long-term (2021-2022) performance of the second-party rain gauge is  
71 evaluated against the national weather stations to qualify as a trusted reference sensor for the  
72 study. Then, an event analysis is performed by calculating evaluation metrics for each sensor  
73 compared with the reference. Data from the radars and third-party sensors require pre-  
74 processing and quality control to facilitate the analysis.

75 XWR are more low-cost compared with conventional C-band and S-band weather radars and  
76 provide higher resolution imagery. They are on the other hand more affected by attenuation,  
77 especially in widespread heavy rainfalls due to the accumulated attenuation throughout the  
78 signal path (Lengfeld et al., 2016; Bobotová et al., 2022). XWR also have a shorter observation  
79 range than conventional radars, typically 30-60 km (Thorndahl et al., 2017). CML are radio  
80 links between base stations that connect the backbone of telecom networks to local  
81 subnetworks (Chwala & Kunstmann, 2019). CML operate at frequencies where the  
82 propagation of radio waves through the atmosphere is attenuated by rainfall. The transmitted  
83 signal level (TSL) and received signal level (RSL) are collected by telecom companies for  
84 network monitoring and maintenance purposes, so what is being considered as “noise” in  
85 telecommunication can be used as a signal to estimate rainfall intensities for  
86 hydrometeorological applications (Leijnse et al., 2007b).

87 A fundamental characteristic of CML observations is that they measure path-integrated rainfall,  
88 generally assumed to represent the average rainfall intensity along the CML path. The validity  
89 of this assumption has, however, been little investigated empirically. In this paper we study the  
90 spatial variability of rainfall along a CML link by sampling XWR bins every 250 meters along  
91 the CML reach, resulting in 20 XWR time series that are compared with the CML rainfall  
92 estimates. This approach enables us to perform new investigations about bias in CML  
93 observations due to variability of rainfall intensity along a CML path.

94 PWS are weather stations installed by occupants on their private property. Here, we consider  
95 PWS that can be connected to online platforms to share observations openly in real time.  
96 Recent years have seen a remarkable increase of PWS connected to the internet, presumably  
97 due to the adoption of smart home technologies (Sovacool & Furszyfer Del Rio, 2020).  
98 Contrarily to CML, PWS are designed to measure rainfall directly, but it can be assumed that  
99 PWS data are subject to errors and bias linked to hardware, installation site and maintenance  
100 (Boonstra, 2024). Various quality control protocols designed specifically for PWS have been  
101 presented by literature (de Vos et al., 2019; Bárdossy et al., 2021; Lewis et al., 2021). However,  
102 it has not been investigated how the algorithms perform when applied to localized extreme  
103 rainfall. In this paper we apply an adjusted version of the PWS quality control protocol  
104 suggested by de Vos et al. (2019) and compare the results with traditional evaluation metrics.



105 This paper addresses multiple gaps in the field of high-resolution rainfall monitoring by 1)  
106 bench-marking second- and third-party sensors with an official monitoring network in the  
107 context of convective rainfall, 2) cross-referencing radar observations with path-integrated  
108 rainfall estimated by CML and 3) investigating the performance of a PWS quality control  
109 protocol in the context of convective rainfall. The study is guided by the following research  
110 questions:

- 111 • To what extent are second- and third-party sensors capable to observe convective  
112 rainfall?
- 113 • What are the advantages and limitations when observing convective rainfall with  
114 second- and third-party sensors, compared with a national monitoring network?

115 This paper is organized as follows. After this introductory section, section 2 presents the storm  
116 event and area of interest that was selected for the case study. Section 3 describes the sensors  
117 and data applied in the analysis. Section 4 presents evaluation metrics and methods applied  
118 for the long-term and event analysis, as well as data processing. Section 5 outlines the results  
119 of the long-term and event analysis. Section 6 discusses the results, while section 7  
120 summarizes the main findings of the study.

## 121 2. Case study

122 A convective rainfall event that hit the Bjäre Peninsula in southwestern Sweden, in the late  
123 afternoon of 18 August 2022, was selected for the study. SMHI's forecast had indicated a small  
124 likelihood of rainfall intensities above 35 mm/3h, which is the institute's threshold for rainfall  
125 weather warnings. However, it was expected to hit further to the North, so no weather warning  
126 was issued in the area at the time of the event. According to media reports, the rain was mixed  
127 with hailstones of about 2 cm in diameter and caused flooding of around 60 buildings  
128 (Gravlund, 2022; Bengtsson, 2023). A local water utility company (NSVA) operates a tipping  
129 bucket rain gauge (hereafter 'municipal gauge') in the city of Båstad, which peaked at 216  
130 mm/h and recorded 75.4 mm in 54 minutes. This corresponds to a return period of about 700  
131 years, based on rainfall statistics developed for southwestern Sweden (Olsson et al., 2019).  
132 The maximum depth recorded in 45 minutes was 71.2 mm, which breaks Sweden's official  
133 record of 61.1 mm in 45 minutes at the *Daglösen* station in Värmland county on 5 July 2000.  
134 The selected event was preceded by two dry days. The analysis focused on the urban area of  
135 Båstad, a town with around 16,000 inhabitants located at the southern coast of the Laholm  
136 Bay, covering approximately 9.4 km<sup>2</sup>. Fig. 1 shows the locations of all sensors included in the  
137 study.

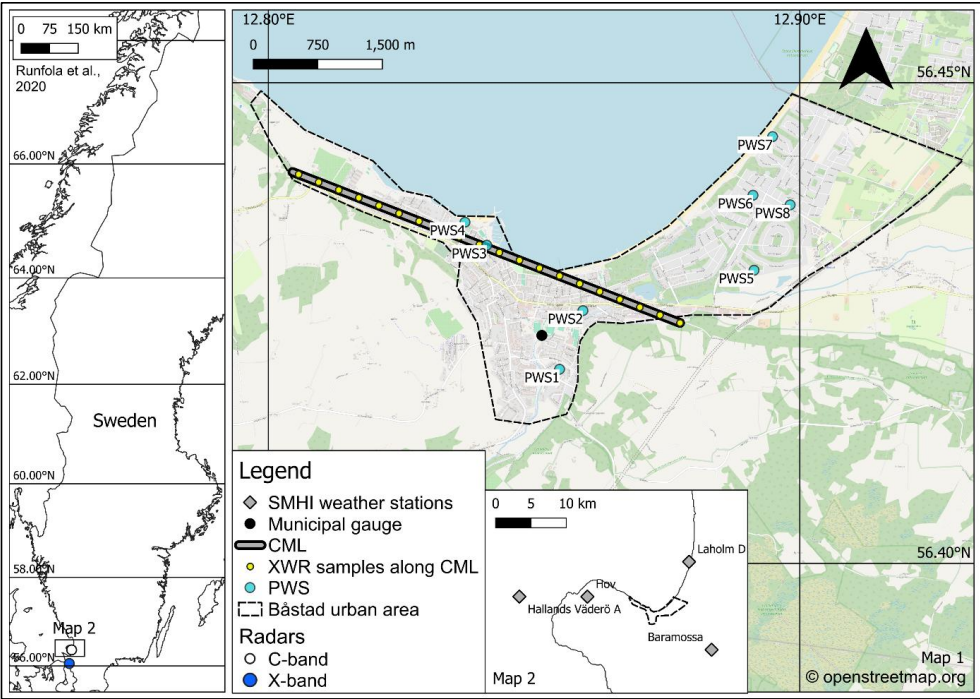


**Figure 1.** Area of interest and locations of sensors. (Runfola et al., 2020).

### 3. Data

Three levels of data were considered in the study – Sweden’s national meteorological monitoring network, a municipal gauge and XWR operated by local and regional agencies (second-party network) and CML and PWS (third-party network). More details on the data sets are provided below.

#### 3.1 National monitoring network

The national weather monitoring network operated by SMHI consists of a combination of manual and automatic weather stations and CWR. The *Hov*, *Laholm D* and *Baramossa* weather stations, located 9-10 km away from Båstad (Fig. 1), report daily accumulated rainfall at 06:00 UTC+2, manually observed by certified observers. The automatic rain gauge station of weighing type on the island *Hallands Väderö*, situated 15 km west of Båstad, report 15-minute accumulations. As these data have passed quality assurance protocols at SMHI, we consider them the most trustworthy source to use for benchmarking in the study. Precipitation data from the stations for the year 2022 was downloaded from SMHI’s open data archive (SMHI, 2025a).

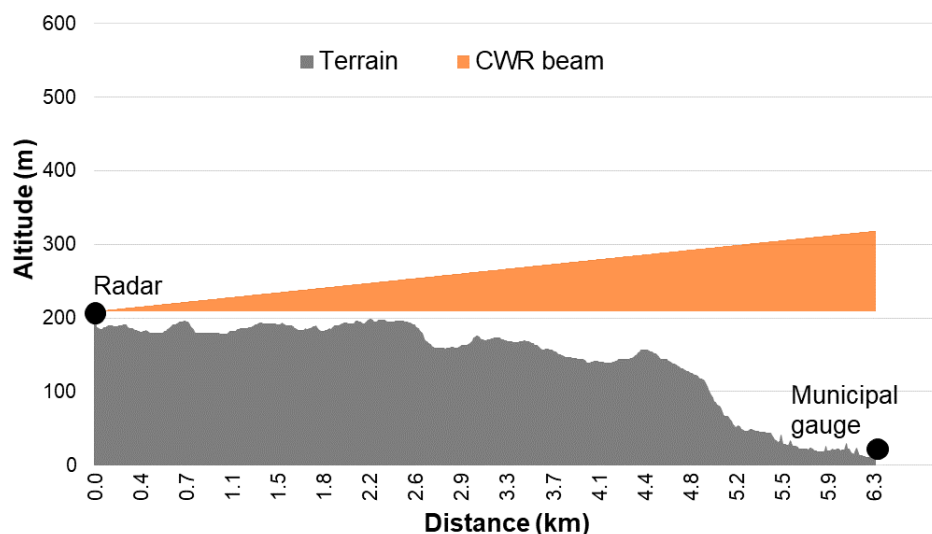


155 In addition, we studied a gauge-adjusted Plan Position Indicator (PPI) radar composite based  
156 on the lowest elevation scan (0.5°) from all radars operated by SMHI. While the radars can  
157 operate in dual-polarization mode, this product is based on the horizontal polarization. Radar  
158 reflectivity  $Z$  [ $\text{mm}^6/\text{m}^3$ ] can expressed as integrals over the Drop Size Distribution (DSD) in the  
159 pulse volume, here  $N(D)$  [ $\text{mm}/\text{m}^3$ ].

$$Z = \int_0^{\infty} D^6(D)N(D)dD \quad (1)$$

160 where  $D$  [mm] is the spherical drop diameter. The closest radar is situated 6 km south of  
161 Båstad, (Fig. 1). Since this radar was operational during the selected event, the studied  
162 composite is based on data from only this radar during the period of interest. The composite is  
163 available in 5 minutes resolution at a spatial resolution of 2x2 km. The compositing of radar  
164 data at SMHI is done with the *BALTRAD* software (*BALTRAD*, n.d.) The composite was  
165 downloaded from SMHI's open radar archive where it is distributed as radar reflectivity data in  
166 GeoTIFF-format (SMHI, 2025b).

167 Figure 2 shows the elevation profile and radar beam profile between the CWR location and the  
168 location of the municipal gauge in Båstad. The low elevation angle and short distance to the  
169 area of interest indicate that the observations are made at approx. 200-300 m above sea level,  
170 eliminating the risk of overshooting, as convective precipitation in the summer months in  
171 Sweden typically originate from much higher altitudes. However, SMHI has experienced partial  
172 beam blockage caused by vegetation within 1 km north of the radar location (SMHI, 2020),  
173 which is known to affect observations over Båstad.



174

175 **Figure 2.** Elevation profile and beam profile between CWR radar location and municipal gauge



## 3.2 Second-party monitoring network

We consider two second-party sensors operated by local and regional authorities; a municipal gauge in Båstad managed by the local water utility company NSVA, and a compact FURUNO dual-polarization XWR operated by NSVA on behalf of Lund University. The municipal gauge is a Casella tipping bucket which records a tip each time the bucket volume (0.2 mm) is filled on 1-second resolution. Time series with 1-minute resolution from the municipal rain gauge for the years 2021-2022 were received upon request from NSVA.

The XWR is located in Helsingborg, 40 km south of Båstad (Fig. 1). The spatial resolution of the data is 0.5 degrees of azimuth and 75 m of slant range at 1-minute time intervals. XWR data for the day of the event was acquired from VeVa (*Weather Radar in the Water Sector*) (VeVa, n.d.), a collaboration between water utility companies in south Sweden and Denmark that distributes XWR data to its partners in according to the EUMETNET Opera Data Information Model (Michelson et al., 2014). The pre-calculated rainfall rate (mm/h) from the lowest scan (elevation angle of 1°) was used, which integrates dual-polarization variables as a method for attenuation correction as described in detail in Hosseini et al. (2020).

Figure 3 shows that the XWR's half-beam vertical profile has a larger sampling volume and steeper elevation angle than CWR (Fig. 2) at the area of interest. As the profile extends 300-1200 meters above sea level over Båstad, this, just like for CWR, suggests a very small risk of signal contamination due to beam blockage and overshooting.

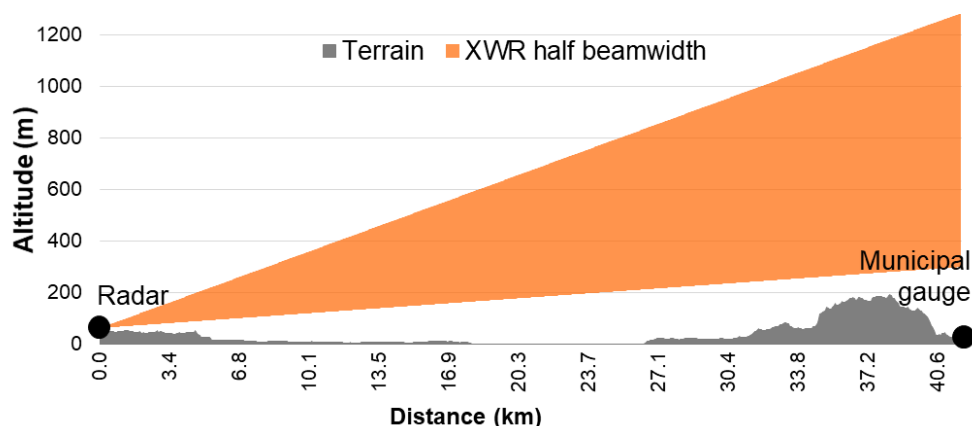


**Figure 3.** Elevation profile and half beam profile between XWR radar location and municipal gauge.

## 3.3 Third-party monitoring network

CML data were received as TSL and RSL at 10 seconds resolution upon request from the telecom companies Ericsson AB and Tre. The data covered all base stations on the Bjäre Peninsula for the days 18-19 August 2022. Each antenna works as both transmitting and





201 receiving terminal, meaning that each link has bidirectional transmission and provides at  
202 least two radio signals. Here, we use the term ‘sub-link’ to refer to a single radio signal. The  
203 location of the only CML in the area of interest is shown in Fig. 1. The link is approximately  
204 4.8 km long. Further details on CML processing is provided in section 4.4.3.

205 The selected PWS type in this study, NetAtmo, is an unheated plastic tipping bucket rain gauge  
206 that reports the number of tips through a wireless connection to the accompanying indoor  
207 module (de Vos et al., 2019). The indoor module broadcasts the observations to Netatmo’s  
208 online platform at approximately 5-minute intervals. The default tipping bucket volume is 0.101  
209 mm, or another volume specified by the station owner using the product’s calibration feature.  
210 PWS time series for the study were received from NetAtmo.

## 211 4. Methods

212 The analyses covered two stages – a long-term analysis and an event analysis. This section  
213 first presents the evaluation metrics applied to assess the performance of the sensors in the  
214 study, followed by descriptions of the methods applied in the long-term analysis and event  
215 analysis. Then, the data processing performed on radar and third-party data is described.

### 216 4.1 Evaluation metrics

217 Three evaluation metrics were used to assess the performance of each sensor: Spearman  
218 rank correlation ( $r_s$ ), Root Mean Squared Error (RMSE), and Percent Bias (PBIAS). The  
219 absolute difference in total rainfall depth during the event was also calculated.

220 The Spearman correlation is a non-parametric test that measures the strength of a monotonic  
221 relationship between two variables:

222

$$r_s = 1 - \frac{6 \sum d_i^2}{n(n^2 - 1)} \quad (2)$$

223 where  $d_i$  is the difference between ranks for each pair of values and  $n$  is the number of  
224 observations. The closer to -1 or 1, the better the negative or positive monotonic relationship.  
225 If very low correlations (close to 0) were found, time lags were applied iteratively by shifting  
226 one of the time series a few minutes back or ahead in time to see if this could increase the  
227 correlation. This can be expected when cross-referencing observations of convective storms,  
228 as the highly intermittent nature of rainfall can cause low correlations even if the total rainfall  
229 depth is similar at two nearby locations. As the Spearman correlation does not address the  
230 magnitude of error, it can be complemented with RMSE (Hyndman & Koehler, 2006):

231





$$RMSE = \sqrt{\frac{1}{n} \sum_{i=1}^n (O_i - T_i)^2} \quad (3)$$

232 where  $O_i$  is the reference rainfall and  $T_i$  is the evaluated data. Lower RMSE indicates a better  
233 model performance. Finally, PBIAS quantifies the average bias, where a positive or negative  
234 value suggests an underestimation or overestimation of rainfall depth, respectively (Gupta et  
235 al., 1999):

236

$$PBIAS = 100 \times \frac{\sum_{i=1}^n (O_i - T_i)}{\sum_{i=1}^n O_i} \quad (4)$$

## 237 4.2 Long-term analysis

238 As the magnitude of the selected event was not captured by the national network (see Results)  
239 it was necessary to establish another reliable reference for the event analysis. Consequently,  
240 the long-term (2021-2022) performance of the municipal gauge was evaluated against the  
241 national weather stations by applying the metrics presented in section 4.1. The gauge was  
242 cross-referenced with the manual stations *Hov*, *Laholm D* and *Baramossa* operated by SMHI,  
243 all situated 9.3-9.7 km away (Fig. 1). The station *Hallands Väderö A* was excluded from the  
244 comparison as it is located on an island 15 km west of Båstad. The tips recorded by the  
245 municipal gauge was resampled to daily accumulations between 06:00-05:59 UTC+2, as this  
246 is the sampling frequency of the reference (manual) stations.

## 247 4.3 Event analysis

248 The event analysis was performed by plotting rainfall rate  $P$  and total depth  $D$  observed by the  
249 second- and third-party sensors and calculating the evaluation metrics. The return period of  
250 the event was calculated based on SMHI's climate statistics for southwestern Sweden (Olsson  
251 et al., 2019). Based on performance, it was decided to exclude CWR as reference sensor  
252 (section 5.2.2). The municipal gauge served as reference for the CWR and XWR observations.  
253 After concluding that XWR recorded similar rainfall depth as the municipal rain gauge during  
254 the event, XWR was used as reference for the third-party data to better account for the spatial  
255 variability of the event. XWR data were sampled every 250 m along the reach of the CML to  
256 investigate the variability of rainfall intensity along the link (section 4.4.4). For PWS, a quality  
257 assurance protocol was applied (section 4.4.5).

258 The temporal range of the studied event differed between the sensors as the start and end of  
259 the rainfall occurred at different times in the observed time series. The event start was defined  
260 as the first timestep when it had been raining more than 0.1 mm/h for at least 5 minutes at the  
261 reference sensor and event stop when it had been raining less than 0.1 mm/h for at least 5



minutes. The calculation of evaluation metrics, return periods and accumulated depths were calculated for this temporal range only, to reduce the number of timesteps with zero rainfall in the calculations, which could distort the relationships.

#### 4.4 Data processing

The radars and third-party data required different levels of pre-processing and quality control which are outlined in the following sections.

##### 4.4.1 C-band weather radar

Radar reflectivity  $Z$  (Eq.1) is generally expressed logarithmically as  $dBZ$ .

$$dBZ = 10 \times \log_{10}(Z) \quad (5)$$

The CWR composite retrieved from SMHI's radar archive is distributed as pseudo-dBZ  $E$  (integer 0-255), which was translated to  $dBZ$  by applying gain and offset:

$$dBZ = E \times G + offset \quad (6)$$

where  $G$  is the gain. Here,  $G = 0.4$  and  $offset = -30$  (Michelson et al., 2014). The rain rate  $P_{CWR}$  (mm/h) can be found from the reflectivity following an inverted power law relationship:

$$P_{CWR} = \left( \frac{Z}{a} \right)^{\frac{1}{b}} \quad (7)$$

We applied the parameters suggested by Marshall & Palmer (1948),  $a=200$  and  $b=1.6$ . The actual values of  $a$  and  $b$  can vary greatly depending on the actual DSD, which may be different within and from event to event (Battan, 1981).

The resulting geoTIFF-files were sampled at the location of the municipal gauge and the eight PWS. In this way, time series at 5-minute resolution from the CWR composite were created. The accumulated rainfall  $D_{CWR}$  (mm) was then calculated per point of interest and for the CWR grid. Evaluation metrics were calculated for the duration of the event as recorded by the municipal gauge.

##### 4.4.2 X-band weather radar

For XWR, the manufacturer's built-in precalculated rainfall rate  $P_{XWR}$  (mm/h) on 1-minute resolution was used for the study. The underlying equations for calculating the rainfall rate is generally similar to CWR as described in the previous section. However, a main difference is that XWR uses different coefficients and corrected dBZ based on the dual-polarization variables, which has been shown to be useful for summer precipitation estimations in Sweden (Hosseini et al., 2020, 2023). It is also noted that the XWR data were available in polar bins, that is, range gates at a given elevation and azimuthal angle, in contrary to the



290 regular cartesian grids for the utilized CWR data. Thus, time series were extracted from the  
291 XWR bins closest to the projected locations of interest, accounting for elevation, range  
292 difference and azimuth difference. The sampled points included the municipal gauge, the  
293 eight PWS, and 20 points along the CML path as described in section 4.4.4.

294 A few missing values were found in the XWR time series, which occurred during the most  
295 intense part of the storm. These were filled with linear interpolation. The volumetric data was  
296 gridded into a cartesian grid 500 meters using the *wradlib* Python package (Mühlbauer &  
297 Heistermann, 2024). The accumulated rainfall  $D_{XWR}$  (mm) was then calculated per point of  
298 interest and for the XWR grid. Evaluation metrics were calculated for the duration of the  
299 event as recorded by the municipal gauge.

#### 300 4.4.3 Commercial Microwave Links

301 When estimating rainfall intensity from CML data, the first step is to identify a link-specific  
302 threshold for classification of wet and dry timesteps. The challenge is to detect small rainfall  
303 volumes (true wet periods) without including too many dry periods with strong attenuation  
304 from other causes, such as changes in water vapour content or air temperature (false wet  
305 periods). Several approaches have been suggested in literature (Rayitsfeld et al., 2012;  
306 Wang et al., 2012; Cherkassky et al., 2014; Overeem et al., 2016). Schleiss & Berne (2010)  
307 proposed a simple classification method that considers the rolling standard deviation of the  
308 attenuation, assuming that the variability is small during dry periods and large during wet  
309 periods. The time step is classified as dry if the variability falls below a defined threshold  
310 value, which must be calibrated with secondary observations nearby the link. More recently,  
311 machine learning approaches has shown strong potential to effectively classify wet and dry  
312 timesteps in CML data (Habi & Messer, 2018; Polz et al., 2020; Øydvin et al., 2024).

313 The second step is to define a 'baseline level', that is, RSL during dry weather. This is used as  
314 the reference level for the rain attenuation calculation and is typically based on the signal  
315 attenuation during dry time steps preceding a wet period (Andersson et al., 2022). In addition,  
316 the signal is often corrected for additional attenuation caused by water on the cover of the  
317 antenna, so-called 'wet antenna attenuation' (e.g., Leijnse et al., 2007a, 2008; Graf et al.,  
318 2020). Finally, the corrected attenuation is converted into rain rate using an inverted power law  
319 relationship.

320 Received TSL and RSL were converted into rainfall rate using the MEMO (Microwave-based  
321 Environmental Monitoring) method developed by SMHI (SMHI, 2025c). This method follows  
322 the general steps applied by most CML algorithms as described above. However, the method  
323 does not explicitly correct for wet antenna attenuation, but instead applies a bias correction



324 factor  $CF_A$  based on link length to the derived rain rate  $P_{raw}$  (mm/h) that compensates for the  
325 wet antenna effect:

$$P_{CML} = P_{raw} - (A_{nl} * CF_A) \quad (8)$$

326 Here,  $P_{raw}$  is the uncorrected rainfall intensity and  $A_{nl}$  is the net attenuation. Details on the  
327 processing steps of the MEMO methodology are outlined in Appendix A.

328 The CML included in this study consists of two sub-links. These recorded very similar values,  
329 with a difference in total rainfall depth of 3 mm for the whole event. Thus, the mean rain rate  
330  $P_{CML}$  and mean depth  $D_{CML}$  per timestep of the two sub-links were used in the analysis.  
331 Evaluation metrics were calculated for the duration of the event as recorded by the mean of  
332 20 XWR bins sampled along the CML reach, see further details in the next section.

#### 333 4.4.4 XWR and CML analysis along CML path

334 To investigate how CML observations of extreme rainfall are impacted by spatial variability  
335 along the link, XWR bins were sampled each 250 m along the reach of the CML, resulting in  
336 20 XWR time series on 1-minute resolution (Fig 1.) The mean of the 20 XWR bins  $\bar{P}_{XWR}$  was  
337 used as reference for CML. The 10<sup>th</sup> and 90<sup>th</sup> percentiles were calculated to explore the range  
338 of  $P_{XWR}$  and  $D_{XWR}$  along the CML path. The behaviour of the XWR data along the CML reach  
339 during the intense part of the storm was inspected visually. Hypothesizing that the difference  
340 in XWR and CML observations is related to the XWR variability along the link, an ordinary least  
341 squares analysis was performed on the difference  $\bar{P}_{XWR}$  and  $\bar{P}_{CML}$ , with the XWR standard  
342 deviation as independent variable.

#### 343 4.4.5 Personal Weather Stations

344 PWS data were received as .csv-files and processed into *netCDF*-files following the standards  
345 proposed by Fencil et al., (2024). PWS without a rainfall sensor, and PWS that were offline  
346 during the storm event, were excluded from the analysis. This resulted in a total of eight PWS  
347 located within the Båstad urban area (Fig. 1). For each PWS, the evaluation metrics were  
348 calculated compared with XWR time series sampled at the same location. The PWS timeseries  
349 were processed with a quality control package as described below.

350 Research has shown that the quality of rainfall data from PWS can be improved significantly  
351 by applying quality control and bias correction. The algorithms suggested in literature (see,  
352 e.g. Mandement & Caumont (2020), Lewis et al. (2021), Bárdossy et al. (2021)) typically utilize  
353 the high observation density of PWS by comparing rainfall time series with the performance of  
354 neighbouring stations, referred to as 'buddy checks' by Båserud et al. (2020). De Vos et al.  
355 (2019) developed a quality control protocol for PWS rainfall data in the R programming  
356 language, *PWSQC*. The method does not rely on a primary monitoring network, but flags  
357 suspicious measurements based on the observations from nearby stations. The method has



358 been applied in gauge-adjustment of radar by Nielsen et al. (2024) and Overeem et al. (2024)  
359 and has recently been converted to a Python package, *pypwsqc*, that was applied for the study  
360 (Chwala et al., n.d.).

361 Event time series from the eight PWS were processed with *pypwsqc*. The algorithm applies  
362 three filters utilizing neighbour checks – the Faulty Zeroes filter, High Influx filter, and Station  
363 Outlier filter – to assess the quality of each time step in rainfall time series by comparing with  
364 the records of neighbouring PWS within a user-defined radius (refer to de Vos et al., 2019, for  
365 details). The Faulty Zeroes filter flags timesteps when the evaluated station records zero  
366 rainfall for at least  $n_{int}$  time intervals, while the median of the surrounding rainfall observations  
367 is larger than zero. The High Influx filter identifies unrealistically high rainfall mounts based on  
368 a comparison with the median rainfall of the neighbouring stations. The Station Outlier filter  
369 flags a station as an “outlier” if the Pearson correlation with the median rainfall of neighbours  
370 in a selected evaluation period falls below a set threshold.

371 To improve the performance of the neighbouring checks, data from all PWS within a 10 km  
372 radius around Båstad were considered, which resulted in a total of 58 stations. However, only  
373 results of the 8 PWS within the area of interest were evaluated during the event. To get a better  
374 understanding of the long-term performance of each PWS, the quality control was also applied  
375 for the full year of 2022. The parameters were set to the same values as in the original  
376 publication (de Vos et al., 2019), except  $m_{match}$  and  $m_{int}$ . These parameters control how many  
377 overlapping wet time steps between the evaluated PWS and its neighbours that are needed  
378 within a defined evaluation period to reliably apply the Station Outlier filter. The numbers  
379 proposed by de Vos et al. (2019) were found to be too strict for the PWS dataset in this study,  
380 as the Station Outlier filter could not be applied for very long periods. Instead, the parameters  
381 were adjusted to require less wet time steps during a longer evaluation period. Table 1 shows  
382 the parameter settings used in the quality control.

383 **Table 1.** Parameter settings for PWS quality control. See de Vos et al. (2019) for description of each  
384 parameter.

Parameter	Value
d (m)	10,000
$n_{stat}$	5
$n_{int}$	6
$\Phi_A$ (mm)	0.4
$\Phi_B$ (mm)	10
$m_{int}$	8064
$m_{match}$	100



Y	0.15
---	------

## 5. Results

### 5.1 Long-term analysis

Figure 4 shows daily accumulations from the *Hov*, *Laholm D* and *Baramossa* weather stations and the municipal gauge for the years 2021 and 2022. The plot shows that the municipal gauge recorded significantly less rainfall than *Baramossa* but followed *Hov* and *Laholm D* reasonably well. This may be because the rain gauges in Båstad, Hov and Laholm are all located close to the coast, whereas the records in Baramossa represent an inland climate.

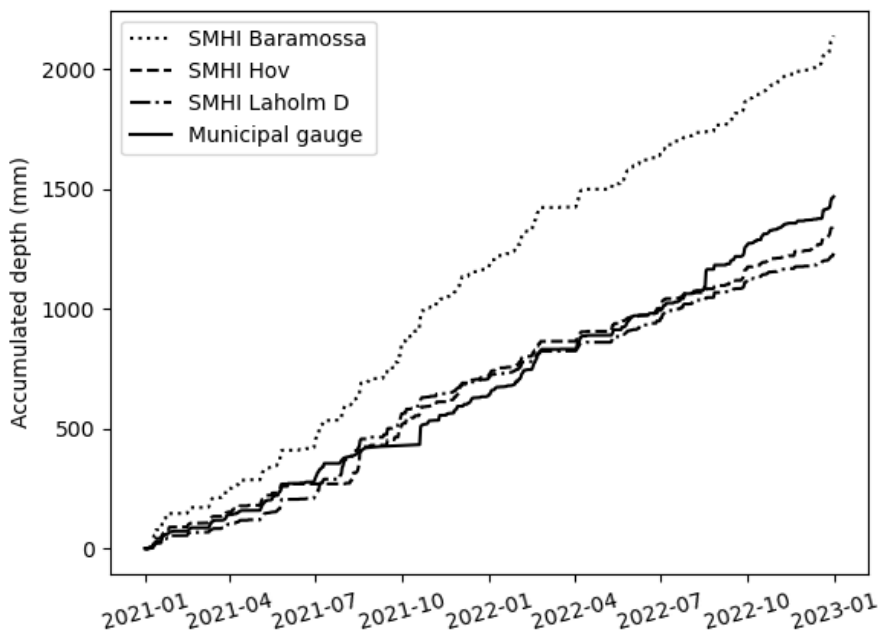


**Figure 4.** Accumulated depth 2021-2022 for municipal gauge and SMHI rain gauges located 9.3-9.7 km away.

Table 2 shows the evaluation metrics of the municipal gauge, benchmarked with the three reference stations. The PBIAS over 2 years was only -8% compared with *Hov* weather station, which is considered low as the stations are situated 9.7 km apart. Based on these results, the municipal gauge was accepted as a trusted reference for the event analysis.



**Table 2.** Cross-validation of the municipal gauge with three reference stations, 2021-2022.

Reference station (SMHI)	Distance to municipal gauge (km)	$r_s$	RMSE (mm/day)	Absolute accumulated difference (mm)	PBIAS (%)
Baramossa	9.4	0.55	6.1	674	31%
Hov	9.7	0.46	5.87	118	-8%
Laholm	9.3	0.52	5.23	233	-19%

## 5.2 Event analysis

### 5.2.1 Event duration

Table 3 summarizes the event duration observed by each sensor. National weather stations were excluded from the analysis, either because they record daily precipitation, or recorded very small total depth (section 5.2.2). The municipal gauge recorded rainfall for 54 minutes, which is among the shortest durations with only PWS 4 observing rain for a shorter period (50 min). Notably, XWR recorded rain for 109 minutes at the location of the municipal gauge. This follows the general pattern that XWR recorded rain for a longer period than the corresponding gauge. The difference was generally around 30 minutes, possibly due to the higher sensitivity of XWR to light drizzles, either never reaching the ground or slowly accumulating in the tipping bucket before the first tip was recorded at the weather station. Comparing XWR with CML, there was only 4 minutes difference in observed event start.

The PWS are concentrated in two clusters. PWS 1-4 are located in the western and central part of Båstad together with the municipal gauge, and PWS 5-8 in the north-eastern part (Fig 1). In Table 3 it can be seen that ground observations in the mid-western part of Båstad started recording rain between 16:55 and 17:15, and the north-eastern part between 17:15 and 17:25, which suggests a gradual motion of the storm from west/south-west to the north-east. A similar tendency is seen in the XWR data, but with approximately 30 minutes time lag.

**Table 3.** Event duration observed by each sensor.

Sensor	Type	Event start (UTC+2)	Event end (UTC+2)	Duration (min)
Municipal gauge	reference	17:15	18:09	54
XWR at municipal gauge	test	16:45	18:34	109
CWR at municipal gauge	test	16:45	17:55	70
XWR mean along CML	reference	16:38	18:36	118
CML mean	test	16:34	18:43	129
XWR at PWS 1	reference	16:40	18:30	110
PWS 1	test	17:05	18:30	85





XWR at PWS 2	reference	16:45	18:30	105
PWS 2	test	17:10	18:30	80
XWR at PWS 3	reference	16:40	18:30	110
PWS 3	test	16:55	18:10	75
XWR at PWS 4	reference	16:40	18:10	90
PWS 4	test	16:55	17:45	50
XWR at PWS 5	reference	16:45	18:35	110
PWS 5	test	17:25	20:00	155
XWR at PWS 6	reference	16:45	18:35	110
PWS 6	test	17:15	18:35	80
XWR at PWS 7	reference	16:50	18:35	105
PWS 7	test	17:25	18:35	70
XWR at PWS 8	reference	16:45	18:35	110
PWS 8	test	17:20	18:30	70

422

#### 423 5.2.2 National monitoring network

424 The total rainfall depth observed by the national monitoring network is shown in Fig. 5. The  
425 CWR grid size is 2x2 km. The weather station *Hallands Väderö A*, situated 15 km west of  
426 Båstad, record accumulated values every 15 minutes but only observed a total volume of 0.4  
427 mm on the day of the event. The other stations report daily accumulations between 06:00-  
428 05:59 UTC+2, amounting to a maximum depth of 14.2 mm at *Hov*. All observations from  
429 SMHI's gauges corresponded to a return period of less than 1 year (Olsson et al., 2019). The  
430 heaviest rainfall observed by CWR was concentrated to the south of Båstad urban area, with  
431 a maximum total depth of 65 mm, which corresponds to a return period of around 400 years  
432 for a duration of 60 minutes (Olsson et al., 2019). The maximum recorded depth in the area  
433 of interest was 25 mm (to the south-east), which corresponds to a return period of 11 years  
434 for a duration of 60 minutes.

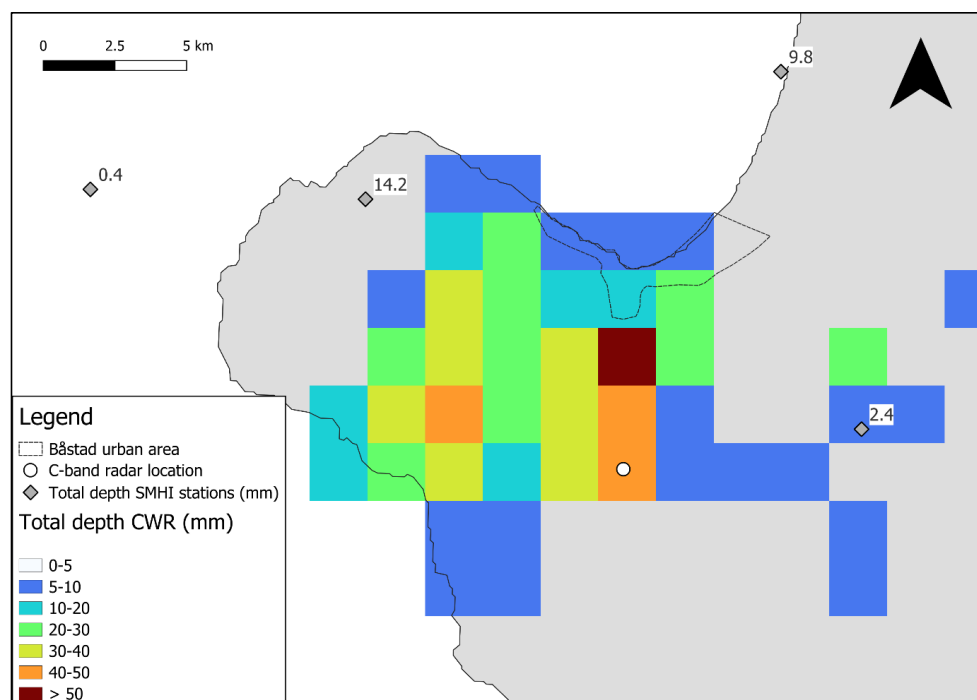
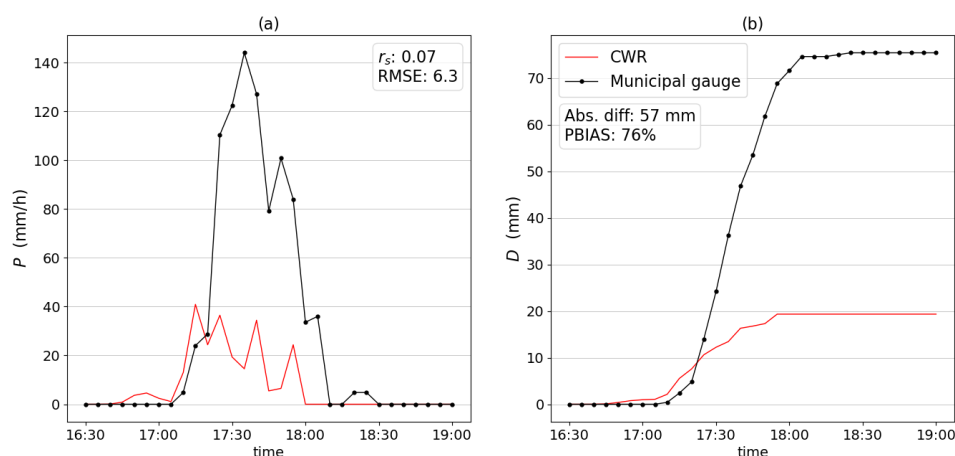


**Figure 5.** Total accumulated depth of the event recorded by the national monitoring network.

Figure 6 shows the rainfall event observed by the municipal gauge, compared with CWR sampled at the same location. CWR underestimated the total depth with 57 mm when comparing with the gauge, which suggest that CWR could not quantify the magnitude of the event accurately. The CWR started to observe rain 30 minutes before the rain gauge. Different time lags were applied to the time series by iteration, and it was found that  $r_s$  could be raised from 0.07 to 0.77 when adding a lag of 25 minutes to the CWR data.



443

444 **Figure 6.** a) Rainfall intensity  $P$  (mm/h), Spearman rank coefficient  $r_s$  (-) and RMSE (mm/5min). b) Total  
445 depth  $D$  (mm), absolute difference in total depth and PBIAS.

### 446 5.2.3 Second-party monitoring network

447 Figure 7 shows the total accumulated depth observed by the second-party network. The  
448 municipal gauge observed rainfall for 54 minutes, between 17:15-18:09, which is here  
449 approximated as 60 minutes. This corresponds to a return period of around 700 years for a  
450 total depth of 75.4 mm (Olsson et al., 2019). The location of the heaviest rainfall was different  
451 when comparing gridded XWR data to the CWR grid. The XWR data indicated two hotspots;  
452 one with total depths above 50 mm in large parts of the Båstad urban area, and one with a  
453 maximum depth of 61 mm 5 km south-west of the city. However, the total depth of XWR  
454 sampled at the location of the municipal gauge based on the closest XWR bin was 78.4 mm,  
455 corresponding to a return period of around 800 years for 60 minutes duration. The total depth  
456 in the gridded XWR data was lower than the point observation because of the averaging that  
457 occurs when interpolating the grid. XWR observations above 5 mm occurred over a much  
458 larger area compared with the CWR, especially to the north-east. This suggests that the CWR  
459 might have been affected by beam blockage during the event.

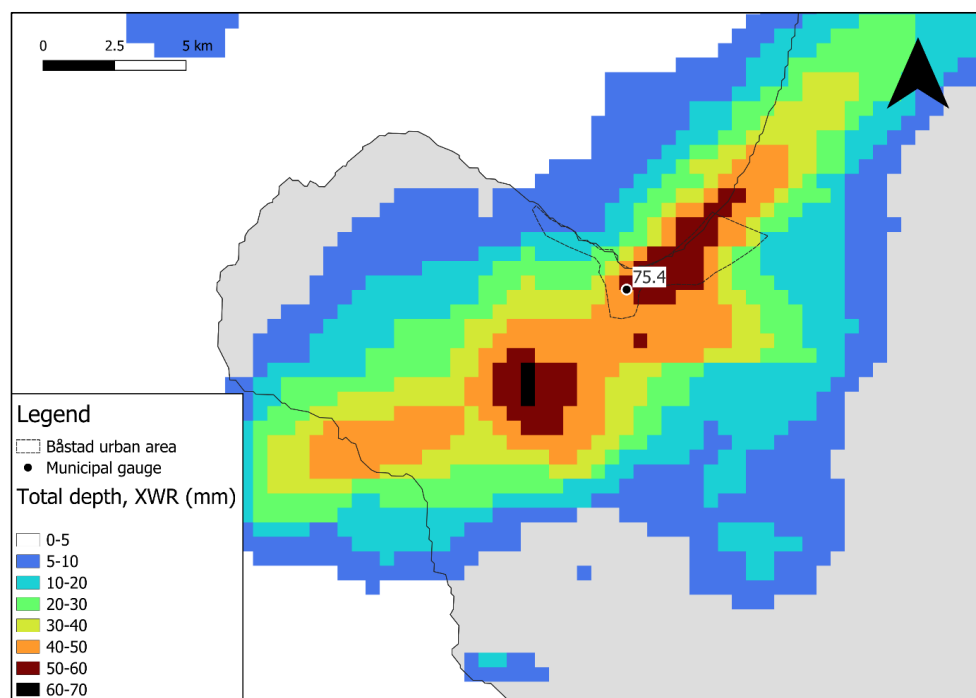


**Figure 7.** Total accumulated depth of the event recorded by the regional monitoring network.

Figure 8 shows the rainfall event observed by the municipal gauge, compared with XWR sampled at the same location. Similar to CWR, the XWR started to record rain almost 30 minutes before the rain gauge. The correlation  $r_s$  could be raised from 0.18 to 0.39 when subtracting a lag of 10 minutes from the XWR data. Even if the correlation was low with the reference, XWR observed a similar total depth with only 3 mm overestimation. In Fig. 8a, it seems that XWR underestimated peak rainfall intensity and overestimated low rainfall intensity. This might be related to signal attenuation during heavy rain and higher sensitivity of XWR to drizzles or observations of melting particles during light rain.

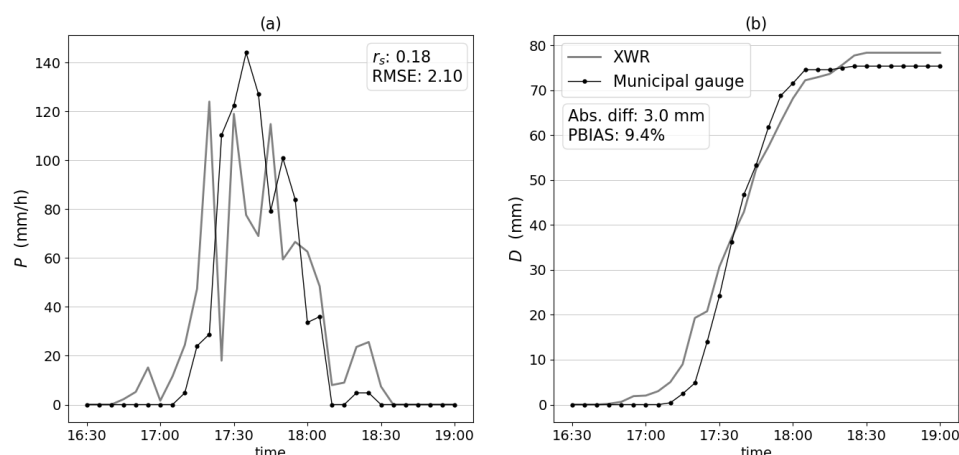


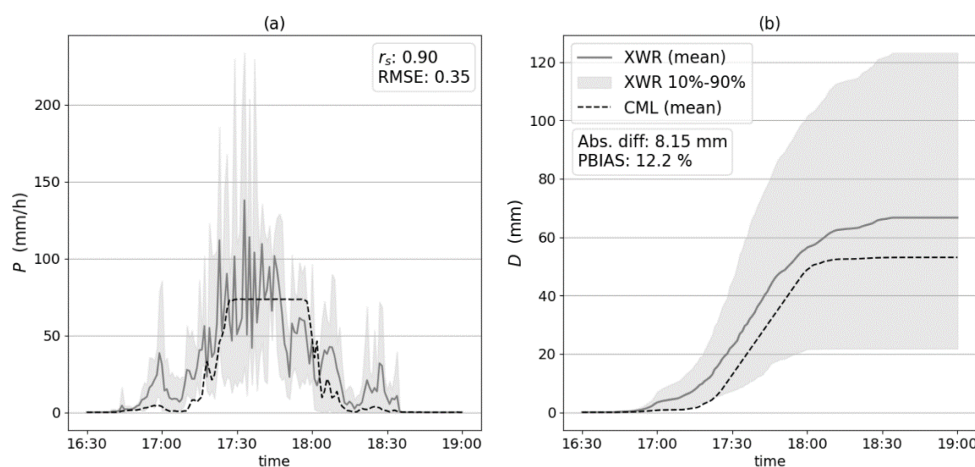
**Figure 8.** a) Rainfall intensity  $P$  (mm/h), Spearman rank coefficient  $r_s$  (-) and RMSE (mm/5min). b) Total depth  $D$  (mm), absolute difference in total depth and PBIAS.

#### 5.2.4 XWR and CML analysis along CML path

Figure 9 shows the rainfall intensity  $\bar{P}_{CML}$  and depth  $\bar{D}_{CML}$  expressed as the mean of the two CML sub-links and the 10<sup>th</sup>-90<sup>th</sup> percentiles of the XWR bins sampled along each 250 m (amounting to 20 sample time series) along the CML path. The mean intensity of the XWR samples  $\bar{P}_{XWR}$  is highlighted in grey and was used as reference for the CML. XWR on average started to observe rainfall at 16:38 along the link path, and CML at 16:43.  $\bar{P}_{CML}$  reached a 'plateau' at 83 mm/h and stayed almost constant at this level for 31 minutes between 17:27-17:58. This effect is caused by complete loss of radio signal between the CML base stations, which is induced by the heavy rainfall, as described by Blettner et al. (2023) and Polz et al. (2023). Despite the plateau, the metrics are remarkably good with high correlation (0.9) and 8 mm total underestimation compared with the reference. The large spread of 10-90<sup>th</sup> percentiles obtained from the 20 XWR observations suggests a large spatial variability of rainfall along the link.



486

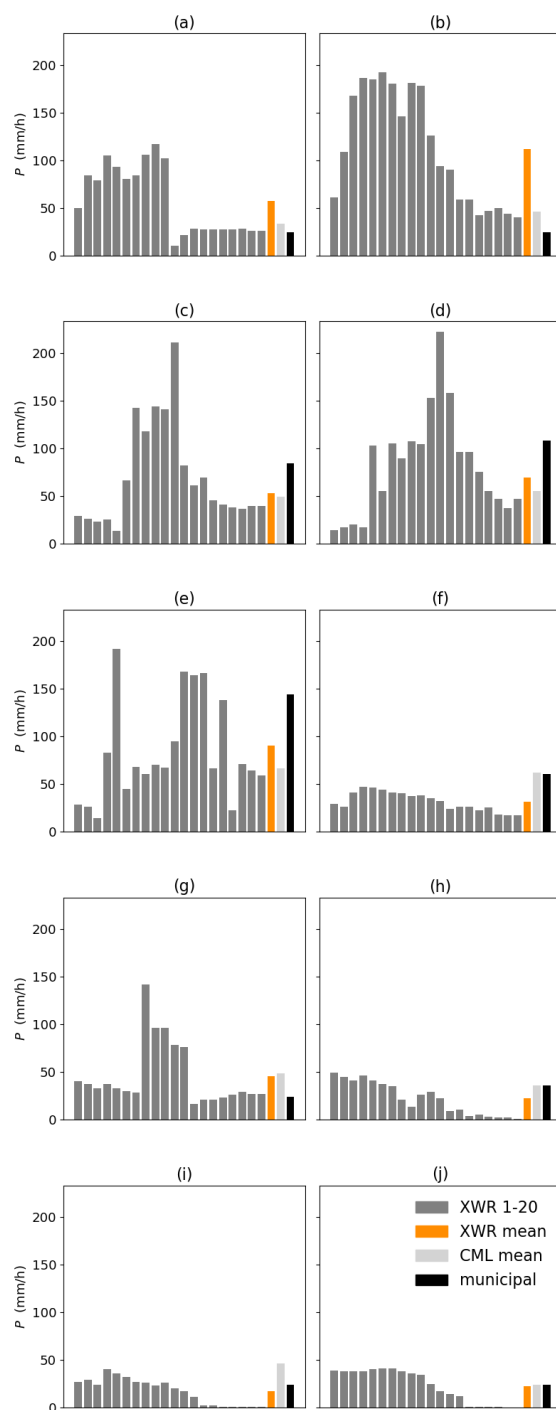


487

488 **Figure 9.** a) Rainfall intensity  $P$  (mm/h) of CML (mean) and XWR (mean and 10<sup>th</sup> to 90<sup>th</sup> percentile)  
489 along CML path. Spearman rank coefficient  $r_s$  (-) and RMSE (mm/min). b) Total depth  $D$  (mm) of CML  
490 (mean) and XWR (mean and 10<sup>th</sup> to 90<sup>th</sup> percentile) along CML path. Absolute difference in total depth  
491 and PBIAS.

492 By inspecting radar fields, it was observed that the storm propagated almost perpendicularly  
493 over the CML link, which is favourable for a detailed comparison between the XWR and CML  
494 observations over the link path. The CML plateau period was considered unsuitable for  
495 comparison, so the following analysis focused on the periods right before and after the signal  
496 loss, from 16:38-17:26 and 17:59-18:36, in total 85 minutes.

497 Figure 10 shows the rainfall intensity distribution along the CML as observed by XWR for five  
498 minutes before and after the plateau. The first bin to the left in the plots was sampled at the  
499 western end of the CML, approximately 3.4 km away from the municipal gauge, and the last  
500 bin to the right was sampled at the eastern end, 1.6 km away from the gauge (see Fig 1.). The  
501 XWR sampling points closest to the rain gauge (bin 14 and 15, counting from the left) are at  
502 approximately 700 meters' distance from the gauge.  $\bar{P}_{CML}$  and  $\bar{P}_{municipal}$  are also shown for each  
503 time step. The XWR spatial distribution was sometimes rather smooth, with gradual increase  
504 and decrease along the link (e.g., Fig. 10b), but sometimes more intermittent, with large  
505 differences between adjacent XWR samples (e.g., Fig 10g). In the pre-plateau period (Fig.  
506 10a-10e)  $\bar{P}_{CML} < \bar{P}_{XWR}$  consistently, whereas in the post-plateau period the relation was  
507 generally the opposite (Fig. 10f-10j).

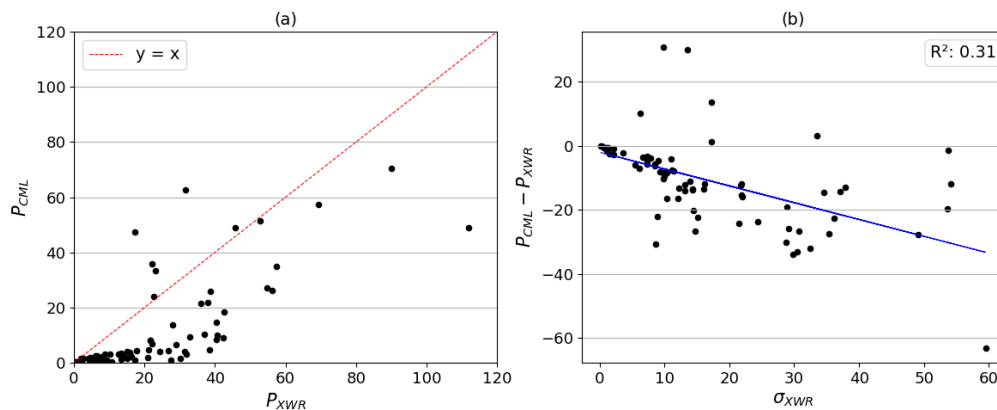






509 **Figure 10.** (a)-(e) Rainfall intensity 5 minutes before CML signal loss (17:22-17:26). (f)-(j)  
510 Rainfall intensity 5 minutes after signal loss (17:59-18:03). Twenty radar bins sampled along  
511 CML path every 250 meters (XWR 1-20), XWR mean, CML mean and municipal gauge.

512 The relationship between  $\bar{P}_{XWR}$  and  $\bar{P}_{CML}$  is shown for all observations in the pre- and post-  
513 plateau periods (in total 85 data points) in Fig. 11a.  $\bar{P}_{CML}$  was generally lower, and especially  
514 when  $\bar{P}_{XWR} < 20$  mm/h, then  $\bar{P}_{CML}$  was consistently very low. This suggests that XWR is more  
515 sensitive to light rain than CML, as was observed when comparing with the municipal gauge  
516 (section 5.2.3). Hypothesizing that the difference between  $\bar{P}_{XWR}$  and  $\bar{P}_{CML}$  was related to the  
517 XWR variability over the link, Fig. 11b shows the difference as a function of the X-band  
518 standard deviation  $\sigma_{XWR}$ . Despite a substantial scatter, a reasonably linear trend is suggested  
519 ( $R^2=0.31$ ) with  $\bar{P}_{CML}$  gradually underestimating more as the standard deviation increases.



520  
521 **Figure 11.** a) Mean rainfall intensity  $P$  (mm/h) along the CML link as estimated by CML and XWR  
522 observations for 85 timesteps. b) Difference between CML and XWR mean intensity values as a function  
523 of XWR standard deviation  $\sigma_{XWR}$  along the CML link.

### 524 5.2.5 Personal Weather Stations

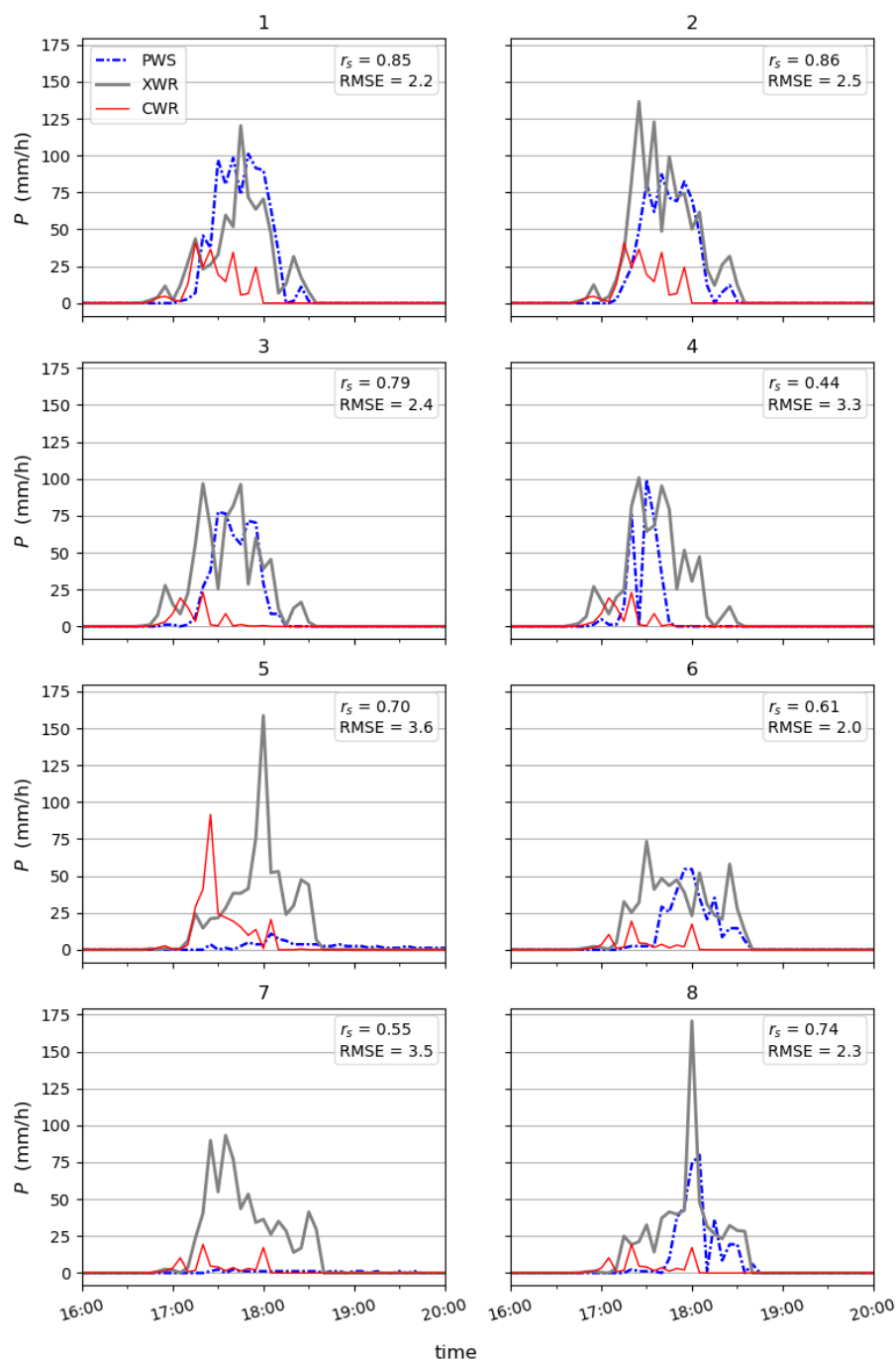
525 This section starts with the results of the PWS quality control, before presenting the event  
526 observations. No faulty zeros or high influxes were detected during the event at any of the  
527 eight PWS in the area of interest. Three of the PWS – PWS 1, PWS 3 and PWS 4 – were  
528 flagged as station outliers. Nevertheless, all PWS were considered for further analysis to  
529 compare the output of the PWS quality control with traditional evaluation metrics. The eight  
530 PWS had between 25 and 29 stations within 10 km radius that were included in the  
531 neighbouring checks.

532 The PWS time series were also checked for the full year 2022. PWS 1 and 4 were flagged as  
533 faulty zeroes continuously during the winter months but had no Faulty Zero flags during the  
534 summer months (see Appendix A, Figure A2). The other PWS got intermittently flagged, but  
535 overall, there were few Faulty Zero flags during the year. No high influxes were detected at



536 any PWS during 2022. All stations were flagged as Station Outliers during extended periods  
537 throughout the year, except one (PWS 6) that only had a few Station Outlier flags in December  
538 2022 (see Appendix A, Fig. A3).

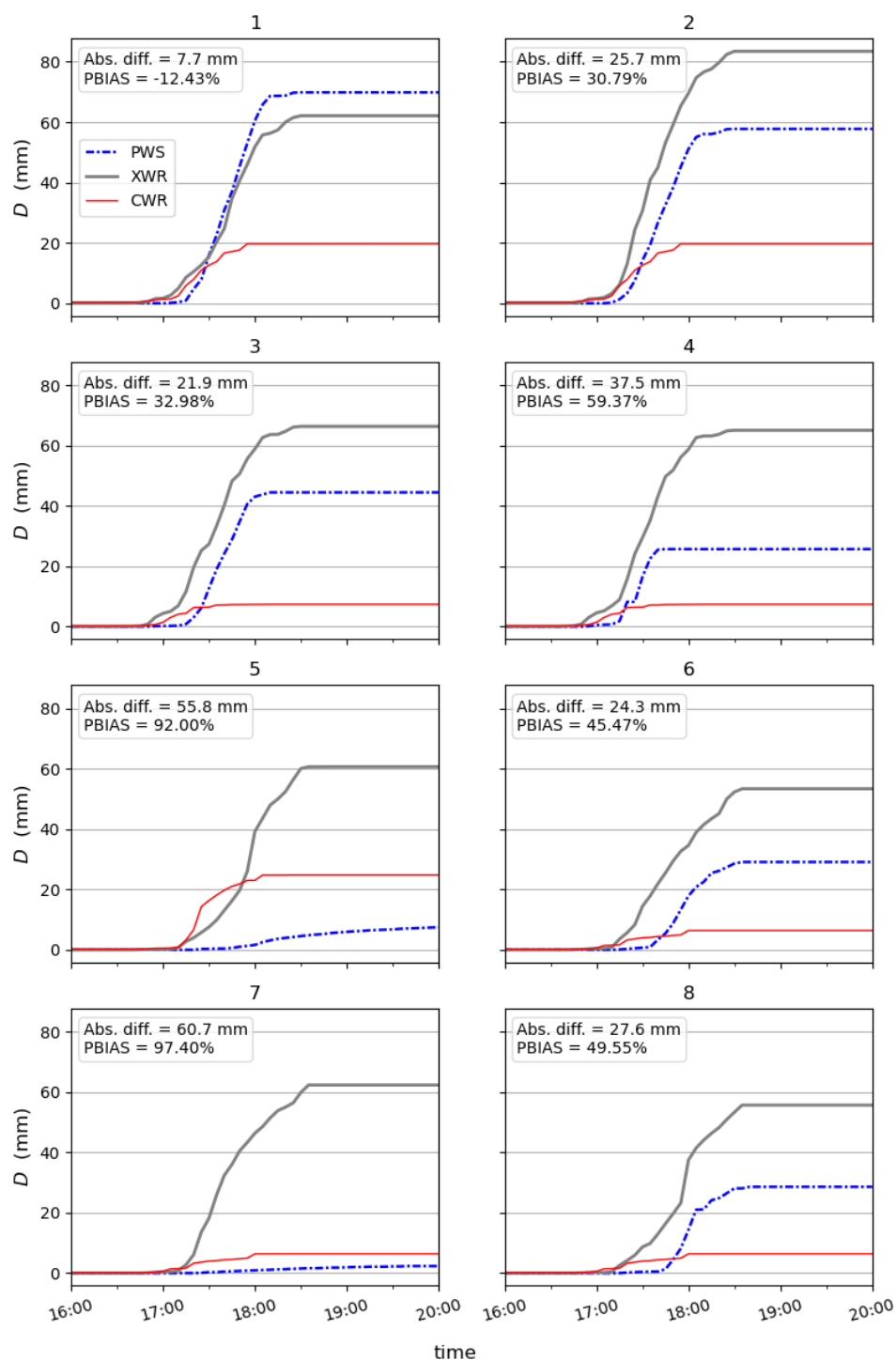
539 Figure 12 shows the rainfall intensity  $P$  (mm/h) observed by the eight PWS and XWR sampled  
540 at the PWS location, with metrics calculated with XWR as reference. The correlation with XWR  
541 was generally quite high, above 0.7 for five of the eight PWS. The CWR sampled at the PWS  
542 locations is included for comparison. Note that the CWR time series are identical for PWS 1  
543 and 2, PWS 3 and 4, and PWS 6, 7 and 8 respectively, meaning that the PWS are situated in  
544 the same CWR grid cell.





546 **Figure 12.** Rainfall intensity  $P$  (mm/h) for PWS 1-8. Spearman rank coefficient  $r_s$  (-) and RMSE  
547 (mm/5min) calculated with XWR sampled at each PWS as reference. CWR sampled at each PWS  
548 included for comparison.

549 Figure 13 shows the accumulated rainfall depth  $D$  (mm) for the event. Almost all PWS  
550 significantly underestimated the total depth compared with XWR reference. However, the  
551 estimate was closer to the reference compared with CWR, with two exceptions (PWS 5 and  
552 PWS 7). PWS 1 is the only PWS that overestimated compared with reference, in total 7.7  
553 mm (PBIAS -12.43%).





555 **Figure 13.** Total depth  $D$  (mm), absolute difference in total depth and PBIAS calculated for PWS 1-8  
556 with XWR sampled at each PWS as reference. CWR sampled at each PWS included for comparison.

## 557 6. Discussion

558 This study investigates the capacity of second- and third-party sensors to observe short-  
559 duration extreme rainfall, compared with a conventional rainfall monitoring network. Sweden's  
560 national rainfall monitoring network, composed of automatic and manual weather stations and  
561 CWR, is used as conventional network in the study. The second-party network consists of a  
562 municipal rain gauge operated by a local water utility company and XWR. CML and PWS are  
563 studied as third-party sensors. First, a long-term analysis of the municipal gauge is performed  
564 by cross-referencing two years of data with the national monitoring network. In this way, the  
565 municipal gauge is established as a trusted reference sensor for the study. Then, a convective  
566 rainfall event that hit southwestern Sweden in the late afternoon of 18 August 2022 is selected  
567 as case study. The event analysis focuses on the urban area of Båstad, a small seaside  
568 municipality on the coast of Laholm Bay, as this location was particularly affected according to  
569 media reports.

570 No weather station in the national monitoring network captured the magnitude of the event as  
571 reported by media. The rainfall observed by the automatic and manual weather stations during  
572 the day of the event corresponded to a return period of less than one year, which suggests  
573 that the rainfall fell between the stations. CWR recorded a maximum total depth corresponding  
574 to a return period of 400 years, but the observation was made south of the Båstad urban area.  
575 Within the area of interest, the maximum recorded depth was only 25 mm, which does not  
576 align with the municipal observations and the media reports about flooded streets and  
577 buildings.

578 CWR peaked at 92 mm/h at 17:25 in the sampling point at PWS 5, which is the only CWR  
579 observation in the expected magnitude of the event based on the municipal gauge. This  
580 suggests that the CWR was affected by partial beam blockage, which has been identified to  
581 be caused by vegetation within 1 km north of the radar location (SMHI, 2020). The  
582 underestimation by CWR may also be attributed to lack of dual-polarization variables and a  
583 dedicated method for attenuation correction. Furthermore, the use of the traditional  $Z-R$   
584 (reflectivity – rain rate) relationship based on Marshall-Palmer coefficients (Marshall & Palmer,  
585 1948) in the CWR data processing may not be well suited for convective storms. SMHI is  
586 currently developing new  $Z-R$  relationships for different weather conditions to improve the  
587 accuracy of CWR-based precipitation estimates in the future.

588 When turning to the second-party data, the magnitude of the event is starting to emerge. The  
589 municipal gauge showed good agreement with the national monitoring network in the long-



term analysis and observed rainfall with a return period of around 700 years in the Båstad urban area. The XWR sampled at the location of the municipal gauge recorded a total depth of 78.4 mm, corresponding to a return period of around 800 years. It must be emphasized that estimated long return periods are highly dependent on the estimated rainfall duration, which may vary significantly in space and are difficult to firmly determine (section 5.2.1). Furthermore, return period estimates are highly uncertain and should therefore not be quantified with high precision. In this context, a difference of ~100 years must be considered relatively small and rather indicate a good agreement between the estimates.

XWR could accurately estimate the total rainfall depth compared with the municipal gauge (PBIAS 9.4%) but showed a low correlation (0.18). The low correlation may be due to differences in the observation height between radar and gauge measurements. During calmer periods of the event, rainfall accumulates gradually in the tipping-bucket gauge until a tip is registered, which can also contribute to the low correlation. XWR observations, particularly at long ranges, are known to be affected by signal attenuation due to interactions with hydrometeors. However, XWR performed well during this event at a 40-km range, likely because the event occurred locally under a mostly clear sky. Remarkably, there was no intervening precipitation between the radar and the target area. Furthermore, it is perceived that overshooting was unlikely due to higher altitude of summer precipitation compared to the XWR sampling volume at the lowest elevation angle. While near-ground radar observations are prone to partial beam blockage, this was likely less of an issue for XWR due to its larger sampling volume and steeper elevation angle compared to CWR, which observed the event from a much shorter distance (6 km).

One CML with a length of 4.8 km is located in the area of interest. The CML correlated well (Spearman coefficient 0.9) with XWR and observed similar duration of the event, which is promising for binary rain/no rain detection. However, the total depth was underestimated compared with the reference as the CML rainfall rate reached a 'plateau' and stayed constant at this level for about 30 minutes. This effect is sometimes referred to as 'blackout' (Polz et al., 2023) and appears when the radio signal is completely attenuated by heavy rainfall (ITU-R, 2005). Telecom network providers design the CML hardware so that transmission outages are allowed to occur 0.01% of the time on an annual basis. Indeed, Polz et al. (2023) found that blackout gaps were present in less than 1% of attenuation data from 4000 CMLs over 3 years in Germany, and that the effect on long-term timescales was generally low. However, the probability of a blackout at rainfall intensities above 100 mm/h was above 40%, which implies that the CML technology currently has limitations in quantifying extreme events.





625 The analysis of XWR data along the CML link revealed some notable result. Firstly, the XWR  
626 data at some time steps exhibited a large bin-to-bin variability, sometimes shifting from one  
627 intensity level to another (Fig 10b). This can be attributed to the turbulent nature of convective  
628 storms, and local attenuations of XWR signals during heavy rain bursts. Despite overall  
629 agreement between  $\bar{P}_{XWR}$  and  $\bar{P}_{CML}$  along the link, a substantial scatter was found where, in  
630 particular, low intensities were consistently higher in the XWR data than CML. Generally, there  
631 was a clear indication that the CML underestimation increased with increasing rainfall intensity  
632 as well as variability along the link. The underestimation observed by both CWR and CML  
633 compared with XWR may partially be explained by XWR's shorter wavelength which interacts  
634 better with small hydrometeors (Lengfeld et al., 2016). Notably, the estimations of the event  
635 duration based on radars and CML was significantly different from the in-situ gauge  
636 observations. For example, the municipal gauge started to observe the event 30 minutes after  
637 CWR. These discrepancies could be attributed to the influence of wind on aloft observations,  
638 larger sensitivity of CML and radars to light rainfall and slow accumulations in the tipping-  
639 bucket gauge during light drizzles preceding the heavy bursts.

640 Regarding the eight PWS in the area of interest, the tipping bucket mechanism seem to have  
641 reached a maximum frequency during heavy moments of the event, as no observation  
642 exceeded 100 mm/h. A similar tendency has been observed by others (Lussana et al., 2023;  
643 Wolf & Larsson, 2024). Among the PWS with lowest RMSE, this led to a PBIAS of 30-40%  
644 compared with XWR reference. PWS 1 performed reasonably well on all evaluation metrics  
645 with a Spearman correlation of 0.9, RMSE 2.2 mm/5min and PBIAS -12.43%. In most cases,  
646 the correlation with reference was medium to high, with only 2 PWS with correlation below 0.6.

647 We applied a quality control specifically designed for PWS rainfall data, *pypwsqc* (Chwala et  
648 al., n.d.) on the event and full year 2022. The algorithm applies three filters – Faulty Zeroes  
649 filter, High Influx filter, and Station Outlier filter – to assess the quality of each time step by  
650 utilizing neighbour checks with nearby stations. No faulty zeroes were detected during the  
651 event, which is reasonable as all PWS in the area of interest measured rainfall at all timesteps.  
652 No high influxes were found, suggesting that all PWS in the area measured enough rainfall not  
653 to trigger high influx flags at the neighbouring stations. On the other hand, no high influx was  
654 detected at any PWS during the entire year 2022. There might indeed not have been any high  
655 influx recorded by any of the 58 PWS on the Bjäre Peninsula in 2022 but the results also raise  
656 the question if the filter parameters should be tuned differently to better capture unrealistically  
657 high inflows.

658 Regarding the Station Outlier filter, three stations were flagged as station outliers during the  
659 event – PWS 1, PWS 3 and PWS 4. However, when inspecting the time series and evaluation  
660 metrics for these stations, it appeared that PWS 1 and PWS 3 had among the highest



661 correlation and lowest RMSE of all PWS and generally showed a reasonable rainfall pattern  
662 compared with the other PWS. These results point to a limitation of neighbouring checks in the  
663 context of convective storms. PWS 1, PWS 3 and PWS 4 are all located in the western part of  
664 Båstad. As such, the Station Outlier filter considered the observations of PWS located further  
665 to the west on the Bjäre Peninsula, which experienced a total depth of only 10 mm according  
666 to the XWR observations. The high spatial variability of the event therefore triggered station  
667 outlier flags at the three PWS located closest to the drier area, even if two of them performed  
668 well when comparing with the XWR reference. If the flagged PWS would have been removed  
669 from further analysis based on the results from the Station Outlier filter, sound observations  
670 would have been lost. Conversely, the performance of PWS 5 and PWS 7 was very poor  
671 compared with the XWR reference, but these stations were not flagged in the automatic quality  
672 control. Future research could explore how the spatial density of PWS and considered  
673 evaluation range influence the capability of neighbour checks to be applicable as quality control  
674 protocols for localized rainfall.

675 The findings of this study align with the well-established fact that national monitoring networks  
676 have limitations in terms of observing convective rainfall. To strengthen capacity in this field,  
677 national meteorological services can include second-party data in operational tools and  
678 workflows. However, differences in acquisition protocols, data formats etc. adopted by different  
679 actors may cause an additional burden and hinder the integration of second-party sensors.  
680 Importantly, southwestern Sweden has an excellent coverage of second-party sensors thanks  
681 to the combination of XWR and rain gauges operated by local authorities, which is certainly  
682 not the case for all points of interest, particularly in countries with limited resources (Winsemius  
683 et al., 2018). In those cases, national meteorological services can turn to third-party sensors,  
684 particularly CML that are typically available in populated settlements across the globe (Chwala  
685 & Kunstmann, 2019; Blettner et al., 2023). However, the results of this study suggest that these  
686 sensors currently have limitations in quantifying the correct magnitude of convective storms.  
687 Still, the results show that third-party data may assist in detecting storm durations and binary  
688 rain/no rain detection.

689 Regarding limitations of the study, a few remarks can be made. First, there are uncertainties  
690 associated with all observations in the study, especially the indirect rainfall measurements  
691 (radars and CML) and the PWS. The long-term assessment of the municipal gauge, combined  
692 with the good agreement between the municipal gauge and XWR, still provide solid evidence  
693 for the actual magnitude of the event. Secondly, some findings are expected to be specific for  
694 this study, such as the low performance by CWR caused by beam blockage in the area of  
695 interest. On the other hand, the underestimation of rainfall observed by the third-party network  
696 aligns with previous studies. It is also expected that quality control protocols that utilize



neighbouring checks will be problematic for other convective storms, depending on the station network density and considered range of the analysis. Although no general conclusions can be drawn from a case study, the depth of this analysis contributes to the understanding of advantages and limitations when observing convective rainfall with second- and third-party sensors.

## 7. Conclusion

This study investigated the capacity of second- and third-party sensors to observe short-duration extreme rainfall compared with a conventional rainfall monitoring network in a case study. The results show that the conventional network was unable to fully capture the event and that second-party sensors can provide accurate and detailed representations of convective storms. However, second-party sensors are not always available, particularly in resource-strained settings. Furthermore, the results suggest that third-party sensors can assist in detecting storm durations and spatial variability of rainfall but have limitations in quantifying the correct magnitude of convective storms. Third-party data may also be difficult to obtain for national meteorological services and has known problems with data quality. Future research is suggested to continue the efforts on quality control of third-party data, especially related to extreme events. In addition, more research is needed on the integration of second- and third-party data in the workflows of national meteorological services.

## Appendix A

### A.1 CML processing

The MEMO (Microwave-based Environmental Monitoring) method was developed and tested on an open data set ('*OpenMRG*') that consists of 364 CML and 11 rainfall gauges in Gothenburg, Sweden, for the period June-August 2015 (Andersson et al., 2022). The processing steps of the MEMO methodology are outlined below.

#### A.1.1 Data pre-processing

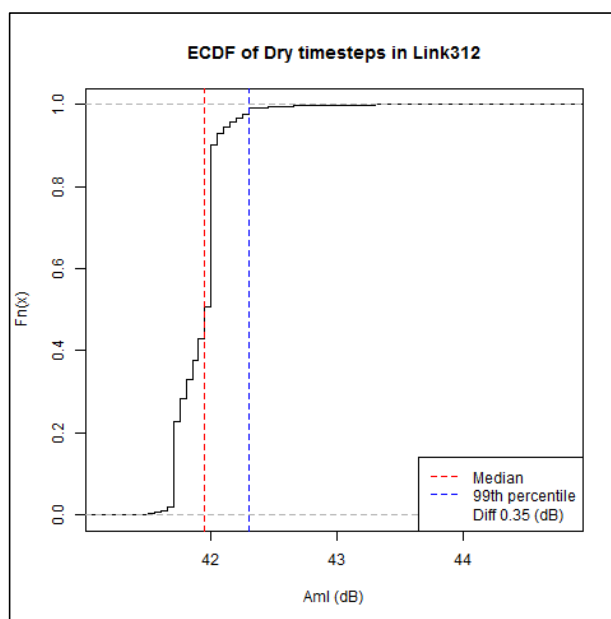
The 10-second attenuation was calculated by taking the difference between TSL and RSL. Then, the median value over a 1-minute period  $A_{m1}$  was taken for all minutes that had more than four 10-second values in one minute and if less data were available, that minute was flagged as missing data.

#### A.1.2 Wet-dry classification

Sub-links in the *OpenMRG* dataset were scrutinized to find a wet-dry classification method that does not rely on secondary observations. The links considered were located within 500 m from a municipal rain gauge in Gothenburg that records at 1-minute temporal resolution, resulting in 72 links. First, dry time steps recorded by the station between 2015-05-14 to 2015-08-31 were considered. A time buffer of 30 minutes was added before and after each rain event



732 recorded by the rain gauge, to consider that rainfall arrives at different timesteps to the links.  
733 The 99<sup>th</sup> percentile of  $A_{ml}$  at dry timesteps identified by the rain gauge was considered to  
734 address that the links may record rainfall that was missed by the rain gauge. Then, the  
735 empirical distribution of  $A_{ml}$  at the dry timesteps was plotted and inspected for the 72 links. An  
736 example is shown in Fig. A1. In this example, the difference between the median and 99<sup>th</sup>  
737 percentile of the attenuation is 0.35 dB.



738

739 **Figure A1.** Example of empirical distribution of attenuation level ( $A_{ml}$ ) at dry timesteps for Link 312.

740 The plots showed that the difference in  $A_{ml}$  between the median attenuation and the 99<sup>th</sup>  
741 percentile was typically between 0.35-0.6 dB at dry timesteps. However, the difference for one  
742 link with considerable fluctuations in signal attenuation was 1.7 dB. Based on these results, it  
743 was decided to set the threshold for the wet-dry classification to the median attenuation over  
744 the past 2 weeks plus an additional 1.7 dB (here called the '*median buffer method*'). In this  
745 study, where only two days of data was available, the median was taken over all available  
746 preceding time steps.

747 The median buffer method was compared with classifying all timesteps with attenuation above  
748 the median of the last two weeks as wet ('*median method*') and the method presented by  
749 Schleiss and Berne (2010) ('*Schleiss method*'), see section 4.4.3. The median method resulted  
750 in overestimation of the number of wet timesteps compared with the rain gauge. The Schleiss  
751 method performed similarly to the median buffer method in correctly identifying the number of



wet timesteps but resulted in some outliers and produced more false wet time steps. Based on these results, the median buffer method was used for further analysis.

#### A.1.3. Baseline definition

The baseline  $A_{bl}$  is the expected difference between TSL and RSL during dry weather. This means that during dry periods, based on the wet-dry classification in the previous step, the baseline is equal to the attenuation  $A_{ml}$ . During wet periods, the baseline is taken as the median of the last  $N$  timesteps from the first wet timestep. A suitable reference period for  $N$  was found to be 240 minutes.

#### A.1.4. Conversion of net attenuation to rain rate

By subtracting the baseline from the attenuation, the net attenuation  $A_{nl}$  was found as

$$A_{nl} = A_{ml} - A_{bl} \quad (A1)$$

Following common practice in CML literature (Leijnse et al., 2007b; Messer et al., 2006), attenuation was converted to rain rate  $P_{raw}$  using the power-law relationship:

$$A_{nl} = kP_{raw}^{\alpha} \quad (A2)$$

The same relationship is used for radar processing, see Eq. 7. In radar literature,  $A_{nl}$  is often expressed as the one-way specific attenuation,  $k$  (dB/km).

The parameters  $k$  and  $\alpha$  depend on link frequency, the polarization state, and the elevation angle of the signal path and was found by applying the equations derived by ITU-R (2005). In contrast to radar scatter, the sensitivity to DSD (Eq.1) is very limited around 30 GHz because  $\alpha$  is approximately 1 in this range, suggesting a nearly linear relation between net attenuation and rain rate (Chwala & Kunstmann, 2019). At frequencies further from 30 GHz, DSD will play a larger role and biases can occur. Most links in Sweden operate near 30 GHz (Andersson et al., 2022).

#### A.1.5 Bias correction based on link length

The derived rain rate was analyzed for the 72 links situated within 500 m range from the 11 rain gauges in the *OpenMRG* dataset for July 2015. When plotting the residuals of the rain rate at the closest gauge against 15-min accumulated net attenuation of the link, a linear relationship was found, indicating potential for bias correction. The slope of the residuals was derived by linear regression for each link and plotted against the link frequency, link length and the parameters  $k$  and  $\alpha$  in Eq. A2. The most distinct relationship was found for link length, suggesting the shorter the length, the higher the slope of the residuals. One probable reason for the relationship is the wet-antenna effect, which is stronger over shorter distances (Chwala & Kunstmann, 2019).



783 It was found that the slope of the regression line of the residuals could be estimated from link  
784 length by applying a simple inverse equation:

$$Slope = f \times \frac{1}{L^g} + h \quad (A3)$$

785 where  $L$  is the link length. The parameters  $f$ ,  $g$  and  $h$  were optimized by minimizing the Mean  
786 Absolute Error for the 72 links, arriving at 2.85214, 1.672 and 0.1615, respectively. The bias  
787 corrected rain rate for the CML in Båstad was then found by calculating the correction factor:

$$CF_A = 2.85214 * (1/L^{1.672}) + 0.1615 \quad (A4)$$

788

789 where  $L$  is 4.8 km in this case. Then, applying the factor to the derived rain rate:

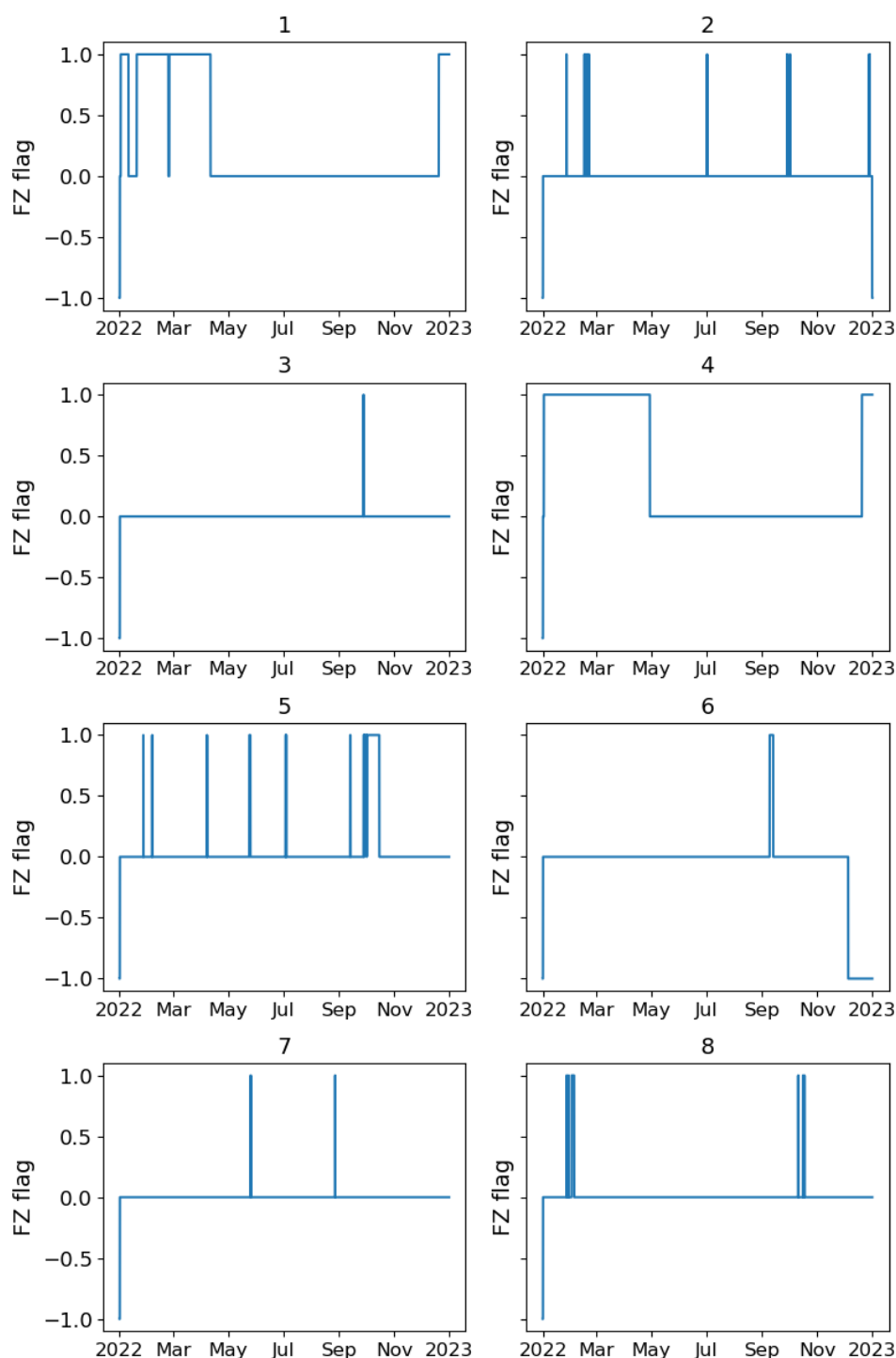
$$P_{CML} = P_{raw} - (A_{nl} * CF_A) \quad (A5)$$

790

## 791 [A.2 PWS quality control 2022](#)

792 Figure A2 shows Faulty Zero (FZ) flags for the eight PWS in the area of interest for the full  
793 year 2022.

794



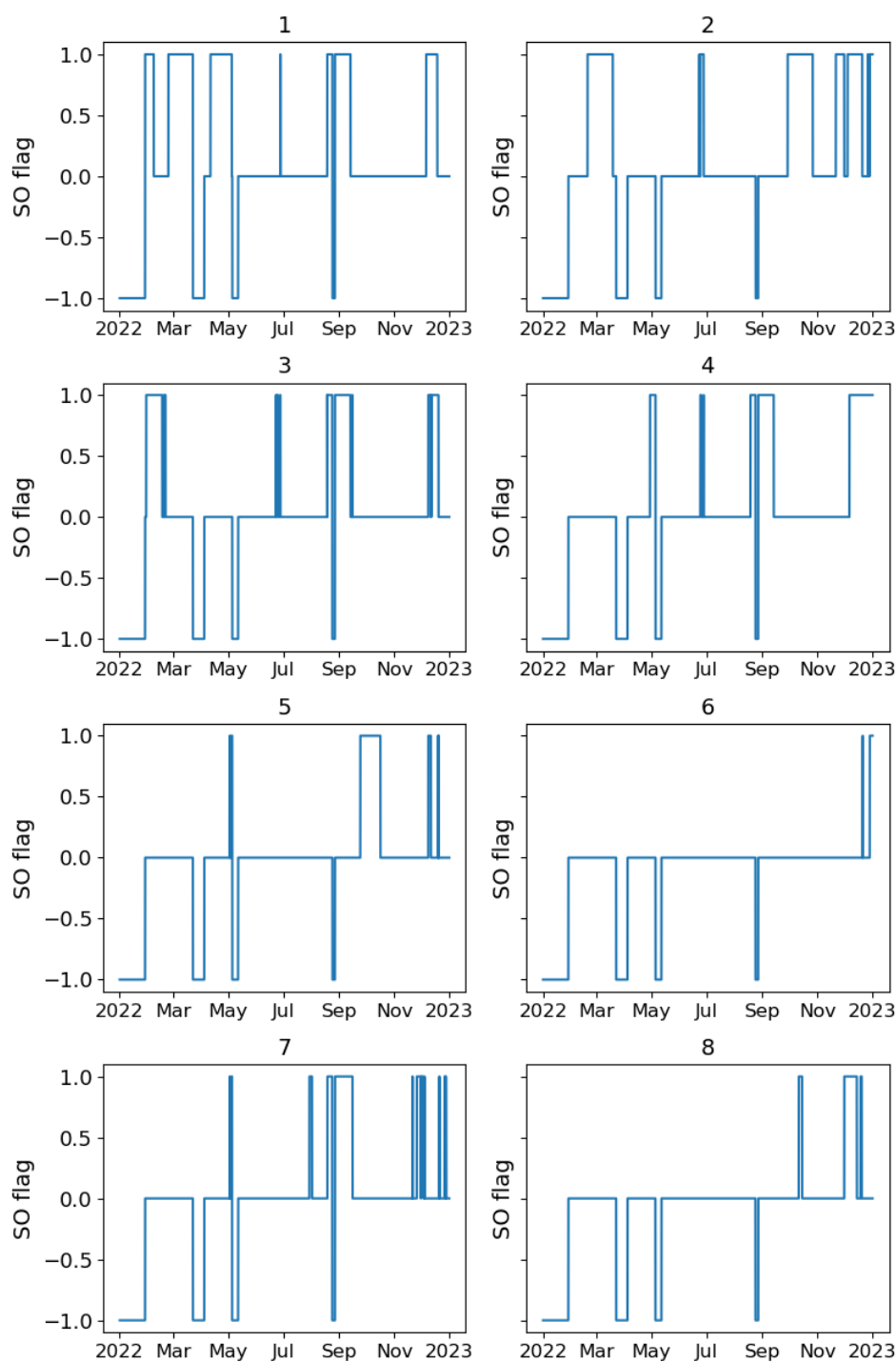
795

796 **Figure A2.** Faulty Zero (FZ) flags 2022. 1 = FZ flag, 0 = no FZ-flag, -1 = FZ-filter could not be applied.





797 Figure A3 shows Station Outlier (SO) flags for the eight PWS in the area of interest for the  
798 full year 2022.



799

800 **Figure A3.** SO-flags 2022. 1 = SO flag, 0 = no SO-flag, -1 = SO-filter could not be applied.



## Data availability

National weather station data and C-band radar composite are available from SMHI's open data archive ([www.smhi.se/data](http://www.smhi.se/data)). The processed national data are available on request. Data from the municipal gauge and X-band radar is property of Nordvästra Skånes Vatten och Avlopp, NSVA. CML data is property of the telecom companies Ericsson AB and Tre. PWS data is property of Netatmo. However, Netatmo data can be openly accessed through their API: <https://weathermap.netatmo.com>

## Author contribution

LPW processed gauge data. LPW and RvdB processed CWR data. HaH, LPW and RvdB processed XWR data. RvdB and LPW processed CML data. JA developed the CML processing methodology. LPW implemented the PWS quality control. LPW, JO and HaH performed data analysis. All authors were involved in the writing and editing of this manuscript.

## Competing Interests

The authors declare that they have no conflict of interest.

## Acknowledgements

The authors would like to thank NSVA for sharing tipping bucket data and Ericsson AB and Tre for sharing CML data. Lennart Simonsson processed PWS data to NetCDF-files. Riejanne Mook improved the CML processing code. The development of *pypwsqc* was carried out jointly with Christian Chwala within the working group 2 of the COST Action OpenSense CA20136.

## Financial support

The paper was supported by the projects SPARC (*Stakeholder participation for climate adaptation – data crowdsourcing for improved urban flood risk management*, grant 2021-02380 Formas) and HyPrecip (*Hyper-resolution multi-dimensional precipitation information for analysis and modelling: urban and rural applications*, grant 2021-01629 Formas). The development of *pypwsqc* received funding from the European Union's Framework Programme for Research & Innovation as part of the COST Action *OpenSense* [CA20136], as supported by the COST Association (European Cooperation in Science and Technology).



## References

- Andersson, J. C. M., Olsson, J., van de Beek, R. (C. Z. ), & Hansryd, J. (2022). OpenMRG: Open data from Microwave links, Radar, and Gauges for rainfall quantification in Gothenburg, Sweden. *Earth System Science Data*, 14(12), 5411–5426. <https://doi.org/10.5194/essd-14-5411-2022>
- BALTRAD. (n.d.). [Computer software]. Retrieved 14 April 2025, from <https://github.com/baltrad>
- Bárdossy, A., Seidel, J., & El Hachem, A. (2021). The use of personal weather station observations to improve precipitation estimation and interpolation. *Hydrology and Earth System Sciences*, 25(2), 583–601. <https://doi.org/10.5194/hess-25-583-2021>
- Båserud, L., Lussana, C., Nipen, T. N., Seierstad, I. A., Oram, L., & Aspelien, T. (2020). TITAN automatic spatial quality control of meteorological in-situ observations. *Advances in Science and Research*, 17, 153–163. <https://doi.org/10.5194/asr-17-153-2020>
- Battan, L. J. (1981). *Radar observation of the atmosphere* (Rev. ed). University of Chicago Press. <https://cir.nii.ac.jp/crid/1130282273102540160>
- Bengtsson, L. (2023). Regn i Båstad. *Vatten: Tidskrift För Vattenvård /Journal of Water Management and Research*, (1-2), 61–70.
- Blettner, N., Fencl, M., Bareš, V., Kunstmann, H., & Chwala, C. (2023). Transboundary Rainfall Estimation Using Commercial Microwave Links. *Earth and Space Science*, 10(8), e2023EA002869. <https://doi.org/10.1029/2023EA002869>
- Bobotová, G., Sokol, Z., Popová, J., Fišer, O., & Zacharov, P. (2022). Analysis of Two Convective Storms Using Polarimetric X-Band Radar and Satellite Data. *Remote Sensing*, 14(10), Article 10. <https://doi.org/10.3390/rs14102294>
- Boonstra, M. M. T. (2024). *Delft Measures Rain. A quality assessment of precipitation measurements from personal weather stations* [Master Thesis, Delft University of Technology]. <https://repository.tudelft.nl/record/uuid:c5720b7e-1828-4948-a76a-89a6361b3e03>



- 856 Cherkassky, D., Ostrometzky, J., & Messer, H. (2014). Precipitation Classification Using  
857 Measurements from Commercial Microwave Links. *IEEE TRANSACTIONS ON*  
858 *GEOSCIENCE AND REMOTE SENSING*, 52(5), 2350–2356.  
859 <https://doi.org/10.1109/TGRS.2013.2259832>
- 860 Chwala, C., & Kunstmann, H. (2019). Commercial microwave link networks for rainfall  
861 observation: Assessment of the current status and future challenges. *WIREs Water*,  
862 6(2), e1337. <https://doi.org/10.1002/wat2.1337>
- 863 Chwala, C., Seidel, J., & Petersson Wårdh, L. (n.d.). *OpenSenseAction/pyowsqc* (Version  
864 v0.1.0 (v0.1.0)) [Python]. Retrieved 19 March 2025, from  
865 <https://doi.org/10.5281/zenodo.14177798>
- 866 de Vos, L. W., Leijnse, H., Overeem, A., & Uijlenhoet, R. (2019). Quality Control for  
867 Crowdsourced Personal Weather Stations to Enable Operational Rainfall Monitoring.  
868 *Geophysical Research Letters*, 46(15), 8820–8829.  
869 <https://doi.org/10.1029/2019GL083731>
- 870 Einfalt, T., Arnbjerg-Nielsen, K., Golz, C., Jensen, N.-E., Quirnbach, M., Vaes, G., & Vieux,  
871 B. (2004). Towards a roadmap for use of radar rainfall data in urban drainage.  
872 *Journal of Hydrology*, 299(3), 186–202. <https://doi.org/10.1016/j.jhydrol.2004.08.004>
- 873 Fencel, M., Nebuloni, R., C. M. Andersson, J., Bares, V., Blettner, N., Cazzaniga, G., Chwala,  
874 C., Colli, M., de Vos, L., El Hachem, A., Galdies, C., Giannetti, F., Graf, M., Jacoby,  
875 D., Victor Habi, H., Musil, P., Ostrometzky, J., Roversi, G., Sapienza, F., ... Zheng, X.  
876 (2024). Data formats and standards for opportunistic rainfall sensors. *Open Research*  
877 *Europe*, 3, 169. <https://doi.org/10.12688/openreseurope.16068.2>
- 878 Fuentes-Andino, D., Beven, K., Halldin, S., Xu, C.-Y., Reynolds, J. E., & Di Baldassarre, G.  
879 (2017). Reproducing an extreme flood with uncertain post-event information.  
880 *Hydrology and Earth System Sciences*, 21(7), 3597–3618.  
881 <https://doi.org/10.5194/hess-21-3597-2017>
- 882 Garcia-Marti, I., Overeem, A., Noteboom, J. W., de Vos, L., de Haij, M., & Whan, K. (2023).  
883 From proof-of-concept to proof-of-value: Approaching third-party data to operational



- 884 workflows of national meteorological services. *International Journal of Climatology*,  
885 43(1), 275–292. <https://doi.org/10.1002/joc.7757>
- 886 Graf, M., Chwala, C., Polz, J., & Kunstmann, H. (2020). Rainfall estimation from a German-  
887 wide commercial microwave link network: Optimized processing and validation for 1  
888 year of data. *Hydrology and Earth System Sciences*, 24(6), 2931–2950.  
889 <https://doi.org/10.5194/hess-24-2931-2020>
- 890 Gravlund, W. (2022, August 19). *Hagel och regnkaos över Båstad: "Aldrig sett något*  
891 *liknande"*. SVT Nyheter. [https://www.svt.se/nyheter/lokalt/helsingborg/kraftiga-skyfall-](https://www.svt.se/nyheter/lokalt/helsingborg/kraftiga-skyfall-over-bastad-har-aldrig-varit-med-om-nagot-liknande)  
892 [over-bastad-har-aldrig-varit-med-om-nagot-liknande](https://www.svt.se/nyheter/lokalt/helsingborg/kraftiga-skyfall-over-bastad-har-aldrig-varit-med-om-nagot-liknande)
- 893 Guo, Y. (2006). Updating Rainfall IDF Relationships to Maintain Urban Drainage Design  
894 Standards. *Journal of Hydrologic Engineering*, 11(5), 506–509.  
895 [https://doi.org/10.1061/\(ASCE\)1084-0699\(2006\)11:5\(506\)](https://doi.org/10.1061/(ASCE)1084-0699(2006)11:5(506))
- 896 Gupta, H. V., Sorooshian, S., & Yapo, P. O. (1999). Status of Automatic Calibration for  
897 Hydrologic Models: Comparison with Multilevel Expert Calibration. *Journal of*  
898 *Hydrologic Engineering*, 4(2), 135–143. [https://doi.org/10.1061/\(ASCE\)1084-](https://doi.org/10.1061/(ASCE)1084-0699(1999)4:2(135))  
899 [0699\(1999\)4:2\(135\)](https://doi.org/10.1061/(ASCE)1084-0699(1999)4:2(135))
- 900 Habi, H. V., & Messer, H. (2018). Wet-Dry Classification Using LSTM and Commercial  
901 Microwave Links. *2018 IEEE 10th Sensor Array and Multichannel Signal Processing*  
902 *Workshop (SAM)*, 149–153. <https://doi.org/10.1109/SAM.2018.8448679>
- 903 Hahn, C., Garcia-Marti, I., Sugier, J., Emsley, F., Beaulant, A.-L., Oram, L., Strandberg, E.,  
904 Lindgren, E., Sunter, M., & Ziska, F. (2022). Observations from Personal Weather  
905 Stations—EUMETNET Interests and Experience. *Climate*, 10(12), Article 12.  
906 <https://doi.org/10.3390/cli10120192>
- 907 Hosseini, S. H., Hashemi, H., Berndtsson, R., South, N., Aspegren, H., Larsson, R., Olsson,  
908 J., Persson, A., & Olsson, L. (2020). Evaluation of a new X-band weather radar for  
909 operational use in south Sweden. *Water Science and Technology*, 81(8), 1623–1635.  
910 <https://doi.org/10.2166/wst.2020.066>



- 911 Hosseini, S. H., Hashemi, H., Larsson, R., & Berndtsson, R. (2023). Merging dual-  
912 polarization X-band radar network intelligence for improved microscale observation of  
913 summer rainfall in south Sweden. *Journal of Hydrology*, 617, 129090.  
914 <https://doi.org/10.1016/j.jhydrol.2023.129090>
- 915 Hyndman, R. J., & Koehler, A. B. (2006). Another look at measures of forecast accuracy.  
916 *International Journal of Forecasting*, 22(4), 679–688.  
917 <https://doi.org/10.1016/j.ijforecast.2006.03.001>
- 918 Imhoff, R. O., Brauer, C. C., Overeem, A., Weerts, A. H., & Uijlenhoet, R. (2020). Spatial and  
919 Temporal Evaluation of Radar Rainfall Nowcasting Techniques on 1,533 Events.  
920 *Water Resources Research*, 56(8), e2019WR026723.  
921 <https://doi.org/10.1029/2019WR026723>
- 922 Kaiser, M., Günnemann, S., & Disse, M. (2021). Spatiotemporal analysis of heavy rain-  
923 induced flood occurrences in Germany using a novel event database approach.  
924 *Journal of Hydrology*, 595, 125985. <https://doi.org/10.1016/j.jhydrol.2021.125985>
- 925 Leijnse, H., Uijlenhoet, R., & Stricker, J. N. M. (2007a). Hydrometeorological application of a  
926 microwave link: 2. Precipitation. *WATER RESOURCES RESEARCH*, 43(4), W04417.  
927 <https://doi.org/10.1029/2006WR004989>
- 928 Leijnse, H., Uijlenhoet, R., & Stricker, J. N. M. (2007b). Rainfall measurement using radio  
929 links from cellular communication networks. *Water Resources Research*, 43(3).  
930 <https://doi.org/10.1029/2006WR005631>
- 931 Leijnse, H., Uijlenhoet, R., & Stricker, J. N. M. (2008). Microwave link rainfall estimation:  
932 Effects of link length and frequency, temporal sampling, power resolution, and wet  
933 antenna attenuation. *Advances in Water Resources*, 31(11), 1481–1493.  
934 <https://doi.org/10.1016/j.advwatres.2008.03.004>
- 935 Lengfeld, K., Clemens, M., Merker, C., Münster, H., & Ament, F. (2016). A Simple Method for  
936 Attenuation Correction in Local X-Band Radar Measurements Using C-Band Radar  
937 Data. <https://doi.org/10.1175/JTECH-D-15-0091.1>



- 938 Lewis, E., Pritchard, D., Villalobos-Herrera, R., Blenkinsop, S., McClean, F., Guerreiro, S.,  
939 Schneider, U., Becker, A., Finger, P., Meyer-Christoffer, A., Rustemeier, E., & Fowler,  
940 H. J. (2021). Quality control of a global hourly rainfall dataset. *Environmental*  
941 *Modelling & Software*, 144, 105169. <https://doi.org/10.1016/j.envsoft.2021.105169>  
942 Lussana, C., Baietti, E., Båserud, L., Nipen, T. N., & Seierstad, I. A. (2023). Exploratory  
943 analysis of citizen observations of hourly precipitation over Scandinavia. *Advances in*  
944 *Science and Research*, 20, 35–48. <https://doi.org/10.5194/asr-20-35-2023>  
945 Mailhot, A., & Duchesne, S. (2010). Design Criteria of Urban Drainage Infrastructures under  
946 Climate Change. *Journal of Water Resources Planning and Management*, 136(2),  
947 201–208. [https://doi.org/10.1061/\(ASCE\)WR.1943-5452.0000023](https://doi.org/10.1061/(ASCE)WR.1943-5452.0000023)  
948 Mandement, M., & Caumont, O. (2020). Contribution of personal weather stations to the  
949 observation of deep-convection features near the ground. *Natural Hazards and Earth*  
950 *System Sciences*, 20(1), 299–322. <https://doi.org/10.5194/nhess-20-299-2020>  
951 Marchi, L., Borga, M., Preciso, E., Sangati, M., Gaume, E., Bain, V., Delrieu, G., Bonnifait, L.,  
952 & Pogačnik, N. (2009). Comprehensive post-event survey of a flash flood in Western  
953 Slovenia: Observation strategy and lessons learned. *Hydrological Processes*, 23(26),  
954 3761–3770. <https://doi.org/10.1002/hyp.7542>  
955 Marshall, J. S., & Palmer, W. M. K. (1948). *THE DISTRIBUTION OF RAINDROPS WITH*  
956 *SIZE*. [https://journals.ametsoc.org/view/journals/atasc/5/4/1520-](https://journals.ametsoc.org/view/journals/atasc/5/4/1520-0469_1948_005_0165_tdorws_2_0_co_2.xml)  
957 [0469\\_1948\\_005\\_0165\\_tdorws\\_2\\_0\\_co\\_2.xml](https://journals.ametsoc.org/view/journals/atasc/5/4/1520-0469_1948_005_0165_tdorws_2_0_co_2.xml)  
958 Michelson, D. B., Lewandowski, R., Szewczykowski, M., Beekhuis, H., & Haase, G. (2014).  
959 *EUMETNET OPERA weather radar information model for implementation with the*  
960 *HDF5 file format, version 2.2* (EUMETNET OPERA Deliverable, 38).  
961 Mobini, S., Nilsson, E., Persson, A., Becker, P., & Larsson, R. (2021). Analysis of pluvial  
962 flood damage costs in residential buildings – A case study in Malmö. *International*  
963 *Journal of Disaster Risk Reduction*, 62, 102407.  
964 <https://doi.org/10.1016/j.ijdrr.2021.102407>





- 965 Mühlbauer, K., & Heistermann, M. (2024). *Wradlib* (Version 2.3.0) [Python].  
966 <https://doi.org/10.5281/zenodo.1209843>
- 967 Nielsen, J. M., van de Beek, C. Z. R., Thorndahl, S., Olsson, J., Andersen, C. B., Andersson,  
968 J. C. M., Rasmussen, M. R., & Nielsen, J. E. (2024). Merging weather radar data and  
969 opportunistic rainfall sensor data to enhance rainfall estimates. *Atmospheric*  
970 *Research*, 300, 107228. <https://doi.org/10.1016/j.atmosres.2024.107228>
- 971 Olsson, J., Södling, J., Berg, P., Wern, L., & Eronn, A. (2019). Short-duration rainfall  
972 extremes in Sweden: A regional analysis. *Hydrology Research*, 50(3), 945–960.  
973 <https://doi.org/10.2166/nh.2019.073>
- 974 Overeem, A., Leijnse, H., & Uijlenhoet, R. (2016). Two and a half years of country-wide  
975 rainfall maps using radio links from commercial cellular telecommunication networks.  
976 *WATER RESOURCES RESEARCH*, 52(10), 8039–8065.  
977 <https://doi.org/10.1002/2016WR019412>
- 978 Overeem, A., Leijnse, H., van der Schrier, G., van den Besselaar, E., Garcia-Marti, I., & de  
979 Vos, L. W. (2024). Merging with crowdsourced rain gauge data improves pan-  
980 European radar precipitation estimates. *Hydrology and Earth System Sciences*, 28(3),  
981 649–668. <https://doi.org/10.5194/hess-28-649-2024>
- 982 Øydvin, E., Graf, M., Chwala, C., Wolff, M. A., Kitterød, N.-O., & Nilsen, V. (2024). Technical  
983 note: A simple feedforward artificial neural network for high-temporal-resolution rain  
984 event detection using signal attenuation from commercial microwave links. *Hydrology*  
985 *and Earth System Sciences*, 28(23), 5163–5171. [https://doi.org/10.5194/hess-28-](https://doi.org/10.5194/hess-28-5163-2024)  
986 [5163-2024](https://doi.org/10.5194/hess-28-5163-2024)
- 987 Petersson, L., ten Veldhuis, M.-C., Verhoeven, G., Kapelan, Z., Maholi, I., & Winsemius, H.  
988 C. (2020). Community Mapping Supports Comprehensive Urban Flood Modeling for  
989 Flood Risk Management in a Data-Scarce Environment. *Frontiers in Earth Science*, 8.  
990 <https://doi.org/10.3389/feart.2020.00304>
- 991 Polz, J., Chwala, C., Graf, M., & Kunstmann, H. (2020). Rain event detection in commercial  
992 microwave link attenuation data using convolutional neural networks. *Atmospheric*



- 993            *Measurement Techniques*, 13(7), 3835–3853. <https://doi.org/10.5194/amt-13-3835->  
994            2020
- 995    Polz, J., Graf, M., & Chwala, C. (2023). Missing Rainfall Extremes in Commercial Microwave  
996            Link Data Due To Complete Loss of Signal. *Earth and Space Science*, 10(2),  
997            e2022EA002456. <https://doi.org/10.1029/2022EA002456>
- 998    Pulkkinen, S., Nerini, D., Pérez Hortal, A. A., Velasco-Forero, C., Seed, A., Germann, U., &  
999            Foresti, L. (2019). Pysteps: An open-source Python library for probabilistic  
1000            precipitation nowcasting (v1.0). *Geoscientific Model Development*, 12(10), 4185–  
1001            4219. <https://doi.org/10.5194/gmd-12-4185-2019>
- 1002    Rayitsfeld, A., Samuels, R., Zinevich, A., Hadar, U., & Alpert, P. (2012). Comparison of two  
1003            methodologies for long term rainfall monitoring using a commercial microwave  
1004            communication system. *Atmospheric Research*, 104–105, 119–127.  
1005            <https://doi.org/10.1016/j.atmosres.2011.08.011>
- 1006    Runfola, D., Anderson, A., Baier, H., Crittenden, M., Dowker, E., Fuhrig, S., Goodman, S.,  
1007            Grimsley, G., Layko, R., Melville, G., Mulder, M., Oberman, R., Panganiban, J., Peck,  
1008            A., Seitz, L., Shea, S., Slevin, H., Youngerman, R., & Hobbs, L. (2020).  
1009            geoBoundaries: A global database of political administrative boundaries. *PLOS ONE*,  
1010            15(4), e0231866. <https://doi.org/10.1371/journal.pone.0231866>
- 1011    Schleiss, M., & Berne, A. (2010). Identification of Dry and Rainy Periods Using  
1012            Telecommunication Microwave Links. *IEEE Geoscience and Remote Sensing Letters*,  
1013            7(3), 611–615. *IEEE Geoscience and Remote Sensing Letters*.  
1014            <https://doi.org/10.1109/LGRS.2010.2043052>
- 1015    SMHI. (2020). *Trädtoppar orsakar blockeringar för väderadar Ängelholm—SMHI*.  
1016            <https://www.smhi.se/nyheter/nyheter/2020-11-20-tradtoppar-orsakar-blockeringar-for->  
1017            [vaderradar-angelholm](https://www.smhi.se/nyheter/nyheter/2020-11-20-tradtoppar-orsakar-blockeringar-for-vaderradar-angelholm)
- 1018    SMHI. (2025a). *Nederbörd*. SMHI. [https://www.smhi.se/data/nederbord-och-](https://www.smhi.se/data/nederbord-och-fuktighet/nederbord)  
1019            [fuktighet/nederbord](https://www.smhi.se/data/nederbord-och-fuktighet/nederbord)



- 1020 SMHI. (2025b, January 9). *Radarbilder, aktuella och historiska*. SMHI.  
1021 <https://www.smhi.se/data/nederbord-och-fuktighet/nederbord/radarbilder-aktuella->  
1022 [och-historiska](https://www.smhi.se/data/nederbord-och-fuktighet/nederbord/radarbilder-aktuella-och-historiska)
- 1023 SMHI. (2025c, February 28). *MEMO*. SMHI. [https://www.smhi.se/en/research/about-us/open-](https://www.smhi.se/en/research/about-us/open-access-to-data-for-research-and-development/memo)  
1024 [access-to-data-for-research-and-development/memo](https://www.smhi.se/en/research/about-us/open-access-to-data-for-research-and-development/memo)
- 1025 Sovacool, B. K., & Furszyfer Del Rio, D. D. (2020). Smart home technologies in Europe: A  
1026 critical review of concepts, benefits, risks and policies. *Renewable and Sustainable*  
1027 *Energy Reviews*, 120, 109663. <https://doi.org/10.1016/j.rser.2019.109663>
- 1028 Thorndahl, S., Einfalt, T., Willems, P., Nielsen, J. E., ten Veldhuis, M.-C., Arnbjerg-Nielsen,  
1029 K., Rasmussen, M. R., & Molnar, P. (2017). Weather radar rainfall data in urban  
1030 hydrology. *Hydrology and Earth System Sciences*, 21(3), 1359–1380.  
1031 <https://doi.org/10.5194/hess-21-1359-2017>
- 1032 UN-Habitat. (2024). *World Cities Report 2024*. United Nations Human Settlements  
1033 Programme (UN-Habitat). <https://unhabitat.org/wcr/>
- 1034 van de Beek, C. Z., Leijnse, H., Hazenberg, P., & Uijlenhoet, R. (2016). Close-range radar  
1035 rainfall estimation and error analysis. *Atmospheric Measurement Techniques*, 9(8),  
1036 3837–3850. <https://doi.org/10.5194/amt-9-3837-2016>
- 1037 VeVa. (n.d.). *Foreningen VeVa – Vejrradar i vandsektoren*. Retrieved 19 May 2025, from  
1038 <https://veva.dk/>
- 1039 Wang, Z., Schleiss, M., Jaffrain, J., Berne, A., & Rieckermann, J. (2012). Using Markov  
1040 switching models to infer dry and rainy periods from telecommunication microwave  
1041 link signals. *Atmospheric Measurement Techniques*, 5(7), 1847–1859.  
1042 <https://doi.org/10.5194/amt-5-1847-2012>
- 1043 Winsemius, H. C., Jongman, B., Veldkamp, T. I. E., Hallegatte, S., Bangalore, M., & Ward, P.  
1044 J. (2018). Disaster risk, climate change, and poverty: Assessing the global exposure  
1045 of poor people to floods and droughts. *Environment and Development Economics*,  
1046 23(3), 328–348. <https://doi.org/10.1017/S1355770X17000444>



1047    Wolf, T., & Larsson, R. (2024). Privata regnmätare för professionell användning– Test av  
1048            Netatmo regnsensor i Trelleborg och Svedala – Tidskriften Vatten. *Tidsskriften*  
1049            *Vatten*, 3. [https://www.tidskriftenvatten.se/tsv-artikel/privata-regnmatare-for-](https://www.tidskriftenvatten.se/tsv-artikel/privata-regnmatare-for-professionell-anvandning-test-av-netatmo-regnsensor-i-trelleborg-och-svedala/)  
1050            [professionell-anvandning-test-av-netatmo-regnsensor-i-trelleborg-och-svedala/](https://www.tidskriftenvatten.se/tsv-artikel/privata-regnmatare-for-professionell-anvandning-test-av-netatmo-regnsensor-i-trelleborg-och-svedala/)  
1051